From virtual screening hits targeting a cryptic pocket in BACE-1 to a nontoxic brain permeable multitarget anti-Alzheimer lead with disease-modifying and cognition-enhancing effects

Caterina Pont [a], Tiziana Ginex [b], Christian Griñán-Ferré [c], Matthias Scheiner [d], Alexia Mattellone [e], Noemí Martínez [a], Elsa M. Arce [a], Yolanda Soriano-Fernández [c], Marina Naldi [e], Angela De Simone [f], Marta Barenys [g], Jesús Gómez-Catalán [g], Belén Pérez [h], Raimon Sabate [i], Vincenza Andrisano [j], María Isabel Loza [k], José Brea [k], Manuela Bartolini [e], Maria Laura Bolognesi [e], Michael Decker [d], Mercè Pallàs [c], F. Javier Luque [b, **], Diego Muñoz-Torrero [a, *]

[a] Laboratory of Medicinal Chemistry (CSIC Associated Unit), Faculty of Pharmacy and Food Sciences, and Institute of Biomedicine (IBUB), University of Barcelona, Av. Joan XXIII 27-31, E-08028, Barcelona, Spain
[b] Department of Nutrition, Food Science and Gastronomy, Faculty of Pharmacy and Food Sciences, IBUB, and Institute of Theoretical and Computational Chemistry (IQTC), UB, E-08921, Santa Coloma de Gramenet, Spain
[c] Pharmacology Section, Department of Pharmacology, Toxicology and Therapeutic Chemistry, Faculty of Pharmacy and Food Sciences, and Institute of Neuroscience, University of Barcelona, Av. Joan XXIII, 27-31, E-08028, Barcelona, Spain
[d] Pharmaceutical and Medicinal Chemistry, Institute of Pharmacy and Food Chemistry, Julius Maximilian University of Würzburg, Am Hubland, DE-97074, Würzburg, Germany
[e] Department of Pharmacy and Biotechnology, Alma Mater Studiorum University of Bologna, Via Belmeloro 6, I-40126, Bologna, Italy
[f] Department of Drug Science and Technology, University of Turin, I-10125, Torino, Italy
[g] GRET, INSA-UB, and Toxicology Unit, Department of Pharmacology, Toxicology and Therapeutic Chemistry, Faculty of Pharmacy and Food Sciences, University of Barcelona, Av. Joan XXIII 27-31, E-08028, Barcelona, Spain
[h] Department of Pharmacology, Therapeutics, and Toxicology, Autonomous University of Barcelona, E-08193, Bellaterra, Spain
[i] Department of Pharmacy and Pharmaceutical Technology and Physical-Chemistry, Faculty of Pharmacy and Food Sciences, and Institute of Nanoscience and Nanotechnology (IN2UB), University of Barcelona, Av. Joan XXIII 27-31, E-08028, Barcelona, Spain
[j] Department for Life Quality Studies, Alma Mater Studiorum University of Bologna, Corso d'Augusto 237, I-47921, Rimini, Italy
[k] BioFarma Research Group, Centro Singular de Investigación en Medicina Molecular y Enfermedades Crónicas (CIMUS), Universidade de Santiago de Compostela, Av. de Barcelona s/n, E-15782, Santiago de Compostela, Spain

ARTICLE INFO

ABSTRACT

Starting from six potential hits identified in a virtual screening campaign directed to a cryptic pocket of BACE-1, at the edge of the catalytic cleft, we have synthesized and evaluated six hybrid compounds, designed to simultaneously reach BACE-1 secondary and catalytic sites and to exert additional activities of interest for Alzheimer's disease (AD). We have identified a lead compound with potent *in vitro* activity towards human BACE-1 and cholinesterases, moderate Aβ42 and tau antiaggregating activity, and brain permeability, which is nontoxic in neuronal cells and zebrafish embryos at concentrations above those required for the *in vitro* activities. This compound completely restored short- and long-term memory in a mouse model of AD (SAMP8) relative to healthy control strain SAMR1, shifted APP processing towards the non-amyloidogenic pathway, reduced tau phosphorylation, and increased the levels of synaptic proteins PSD95 and synaptophysin, thereby emerging as a promising disease-modifying, cognition-enhancing anti-AD lead.

* Corresponding author. Laboratory of Medicinal Chemistry (CSIC Associated Unit), Faculty of Pharmacy and Food Sciences, and Institute of Biomedicine (IBUB), University of Barcelona, Av. Joan XXIII 27-31, E-08028, Barcelona, Spain.
** Corresponding author. Department of Nutrition, Food Science and Gastronomy, Faculty of Pharmacy and Food Sciences, IBUB, and Institute of Theoretical and Computational Chemistry (IQTC), UB, E-08921, Santa Coloma de Gramenet, Spain.
E-mail addresses: fjluque@ub.edu (F.J. Luque), dmunoztorrero@ub.edu (D. Muñoz-Torrero).

1. Introduction

Alzheimer's disease (AD) is the most common type of dementia among the elderly. Affecting more than 35 million people worldwide, out of some 50 million having dementia, AD is the most prevalent neurodegenerative disorder. With the demographic trend towards an increasingly ageing population, the projected prevalence figures of this age-related disorder for the upcoming years are really worrisome and so will be other closely associated factors such as mortality and economic burden unless an effective treatment, capable of halting or slowing down AD progression, is urgently developed [1].

Indeed, the turning point of the dramatic socioeconomical impact of AD would be the discovery of new drugs that hit the mechanisms that underlie neurodegeneration, going beyond the symptomatic effects of the few currently available drugs. After two decades of fruitless drug discovery endeavors addressing one or another particular disease mechanism, such as amyloid pathology, tau pathology, cholinergic or other neurotransmitter deficits, oxidative stress, or biometal dyshomeostasis, it is becoming increasingly apparent that the most realistic way to cope with this complex multifactorial disease would involve the development of multitarget drugs or combinations of drugs that enable the simultaneous modulation of multiple key AD targets or pathological events [2–4]. Indeed, the design of multitarget compounds, mainly by hybridization of different pharmacophores, has experienced an exponential growth in the past fifteen years and is a focus of very intensive research [5–14].

In this arena, we recently reported the development of the multitarget compound **1** (Fig. 1), as the lead of a novel class of hybrids that combine the scaffold of the natural product rhein, closely related to some hydroxyanthraquinones with tau anti-aggregating activity [15], and that of the potent acetylcholinesterase (AChE) inhibitor huprine Y (**2**, Fig. 1) [16,17]. Apart from the expected activities at the primary targets, AChE and tau aggregation, and the related butyrylcholinesterase (BChE) and β-amyloid (Aβ) antiaggregating activities, a salient feature of the rhein–huprine hybrid **1** was a potent *in vitro* activity against the β-site amyloid precursor protein cleaving enzyme 1 (BACE-1 or β-secretase) (Fig. 1) [18].

BACE-1 is widely expressed in the brain, being especially abundant in various neuronal cell types. Its concentration and activity rate are increased in the brains of AD patients, thereby pointing out that BACE-1 is a key pathogenic factor in AD. Together with γ-secretase, BACE-1 cleaves the transmembrane amyloid precursor protein (APP) to generate different Aβ species, with BACE-1-mediated APP cleavage being the rate-limiting step for Aβ production. Actually, BACE-1 is involved in the synthesis of all monomeric forms of Aβ, including the most aggregation-prone and neurotoxic Aβ42, widely regarded as one of the main culprits of AD neurotoxicity. *In vivo* studies in a mouse model of AD highlighted the relevance of the human BACE-1 (hBACE-1) inhibitory activity of compound **1** within its multitarget profile, as this compound led to diminished levels of neurotoxic soluble Aβ oligomers and amyloid deposits, reduced neuroinflammation and tau pathology in cortex and hippocampus, and improved cognition [19].

BACE-1 features an open, very large (volume close to 1000 A^3) and elongated (around 20 Å) flexible active site, which can be regarded as a collection of subsites, including the pocket that contains the catalytic dyad formed by aspartate residues, Asp32 and Asp228 [20]. Notwithstanding this fact, inspection of the available crystal structures of BACE-1 revealed that its binding site was not large enough to accommodate compound **1**. Extended molecular dynamics (MD) simulations, together with pocket druggability studies, led us to detect the transient formation of a secondary binding site, which contained Arg307 as the key interacting residue, at the edge of the catalytic cleft [21]. The huprine moiety of **1**, protonated at the range of pH optimal for BACE-1 activity (pH 2.5–4.5), was predicted to interact with the catalytic dyad, whereas the rhein moiety would be interacting with a so far non described floppy secondary site, mainly through a hydrogen bond between the carbonyl group of the most hydrophobic edge of the rhein moiety and the guanidinium group of Arg307. In the family of rhein–huprine hybrids, a drastic dependence of BACE-1 inhibitory activity on the tether length was observed [18]. The nonamethylene linker of **1** provided the most adequate separation between huprine and rhein moieties to enable the dual site binding within BACE-1, which likely accounts for the potent BACE-1 inhibitory activity of this compound.

A number of BACE-1 inhibitor drug candidates have entered clinical trials in the past years, so far without success. Induction of unwanted side effects is one of the main factors behind these clinical failures [22]. Because BACE-1 can cleave other substrates apart from APP, excessive inhibition of BACE-1 has been proposed to likely account for toxicity issues observed with previous drug candidates, whereas lower levels of inhibition could lead to the desired therapeutic efficacy [23]. Thus, notwithstanding previous failures with BACE-1 inhibitor clinical trials, this enzyme remains a prime well-validated therapeutic target for halting or slowing down AD progression and new potential BACE-1 inhibition strategies are currently pursued [24,25], including BACE-1 inhibitor-based multitarget agents [26,27]. Virtual screening has been successfully employed to discover new hits with moderate BACE-1 inhibitory activity [20,28,29]. The disclosure of the aforementioned druggable transient secondary pocket of BACE-1 in our previous studies [21] paves the way for virtual screening campaigns especially aimed at identifying new fragments that could stabilize the open state of this cryptic pocket. The resulting virtual hits might be then combined with other pharmacophores to design novel multitarget compounds featuring multisite binding within BACE-1 and other activities of interest for AD treatment.

Herein, we describe the discovery of a promising multitarget compound with beneficial effects on cognition and multiple pathologies in a mouse model of AD, which has been identified after: i) a virtual screening campaign directed toward the transient

IC$_{50}$ hAChE = 3.60 nM
IC$_{50}$ hBChE = 620 nM
48% inhibition of Aβ42 aggregation at 10 μM
30% inhibition of tau aggregation at 10 μM
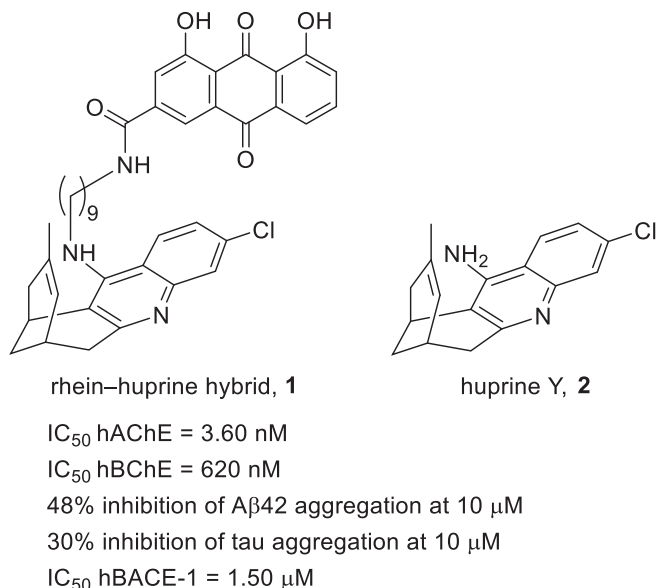IC$_{50}$ hBACE-1 = 1.50 μM

Fig. 1. Chemical structures of rhein–huprine hybrid **1** and the parent huprine Y, **2**.

secondary binding site of BACE-1 that led to the identification of several hits, with smaller size and lower lipophilicity than the rhein moiety of **1**; ii) the synthesis of a series of hybrid compounds, designed by combination of the scaffolds of the BACE-1 secondary site virtual screening hits with a huprine moiety through a nine-carbon linker; iii) the *in vitro* multitarget biological profiling of all compounds toward their primary targets (BACE-1, AChE, BChE, and Aβ42 and tau aggregation) and toward other potential targets, i.e., the assessment of biometal chelating properties and antioxidant activity; iv) the *in vitro* determination of their blood–brain barrier (BBB) permeability and the aqueous solubility; v) the assessment of the potential toxicity of all compounds in two model systems, i.e., zebrafish embryos and mouse hippocampal neuronal HT22 cells; and finally vi) a chronic *in vivo* efficacy study of the lead compound **11** in SAMP8 mice.

2. Results and discussion

2.1. Virtual screening for BACE-1 secondary binding site hit identification

A subset of 283,130 fragments/small compounds initially selected from the ZINC database (see Experimental section for details) was prepared using the LigPrep module of Maestro (Schrödinger suite). This subset was then used in a virtual docking

screening targeting the secondary binding pocket of BACE-1. To this end, two snapshots (model 1 and 2), which mainly differ in the orientation adopted by the side chain of the key Arg307 residue, were taken from the subset of structures sampled in previous molecular dynamics simulations of the BACE-1 complex with compound **1** (Fig. 2) [21]. The virtual screening was performed using the Glide module of the Schrödinger (Maestro) suite. First, a preliminary high-throughput virtual screening (HTVS) was performed using the HTVS GScore function and poses with a GScore > −7.0 kcal/mol were filtered out, keeping 550 and 343 compounds for models 1 and 2, respectively (Supplementary Fig. S1). These compounds were subsequently used in a second virtual screening performed with the extra precision (XP) score function. Only poses with GScore values < −6.50 kcal/mol (94 and 115 compounds for models 1 and 2, respectively) were saved. Visual inspection was then performed in order to check the docking of the fragments in the secondary pocket, particularly regarding the formation of hydrogen bond interactions with Arg307, leading to a subsequent selection of 82 compounds (18 and 64 compounds for models 1 and 2, respectively; Fig. 2 and Tables S1 and S2 in the Supplementary Material).

The final selection of the hits that were incorporated in the novel hybrids was performed by considering those scaffolds that enabled the establishment of additional interactions at the secondary site of BACE-1, apart from the H-bond interaction with
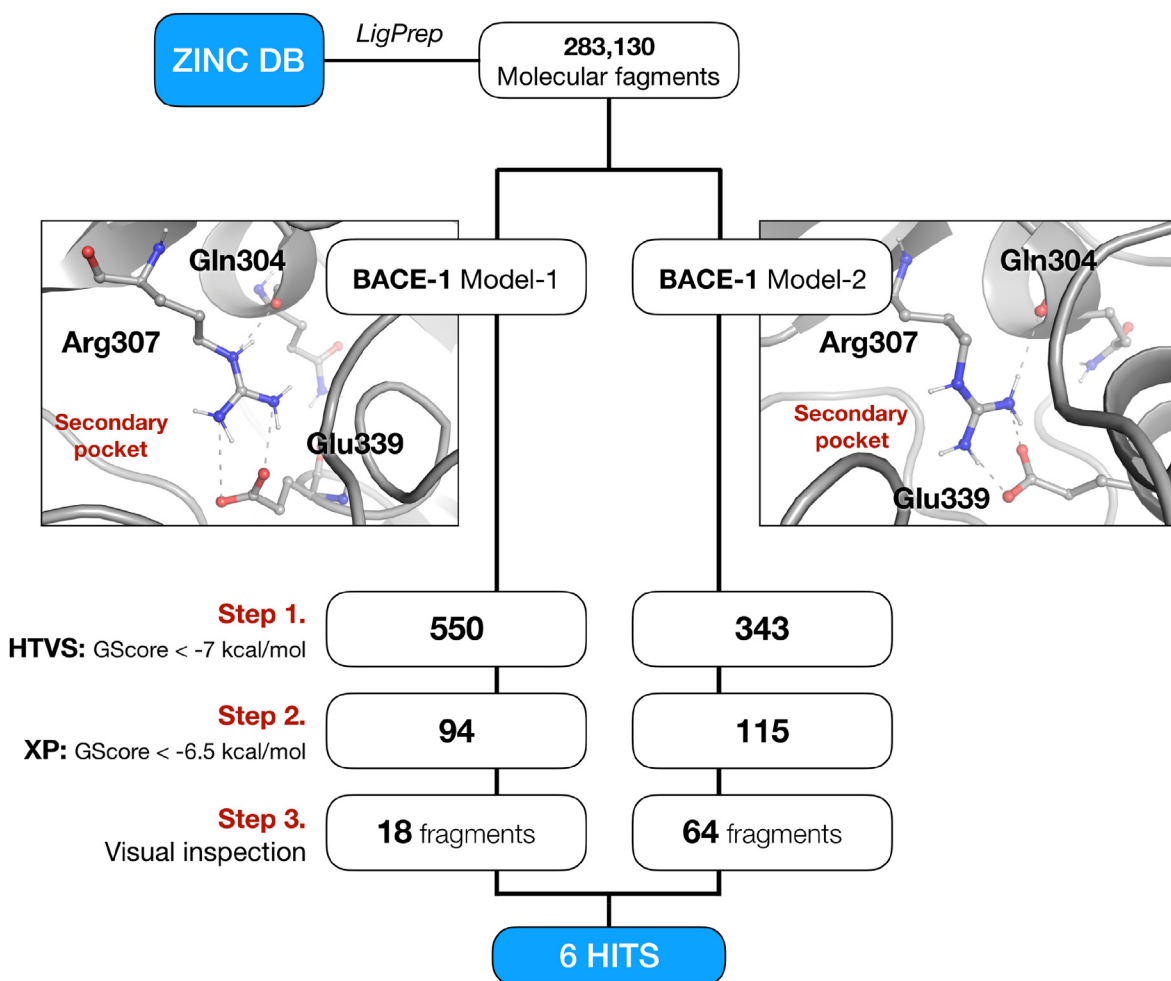

Fig. 2. Virtual screening workflow applied in this study. The plots display the orientation of the Arg307 side chain in the secondary pocket of BACE-1 for the two BACE-1 structural models used in the virtual screening.

Arg307, and the commercial availability of reagents that contained those scaffolds and a suitable functionalization for the eventual attachment to the linker–huprine fragment (see below). This led to a final selection of six virtual screening hits (VSH) (compounds **3**−**8**, Fig. 3). Of note, the scaffolds of the hits **3**, **6** and **7** were over-represented in the set of the 82 previously selected compounds, as they appeared repeatedly in 8, 8 and 44 compounds, respectively (Tables S1 and S2 in the Supplementary Material). Thus, the scaffolds that are present in the VSH **3**−**8** overall covered 63 out of the 82 compounds that were selected upon visual inspection.

The selected VSH **3**−**8** were used for the design of the target hybrids (**9**−**14**, Fig. 3) featuring a huprine moiety and a linker of nine carbon atoms, either a nonylamino or a nonanoyl group, depending on the complementary functionalization of the VSH moiety (a carboxylic or sulfonic acid or an amine, respectively), which were deemed suitable to span the 10 Å distance between the catalytic pocket and the transient secondary site of BACE-1, thereby enabling a dual site binding within this enzyme.

2.2. Synthesis of VSH-based hybrids **9**−**14**

The hybrids **9** and **11** were synthetized through a 3-step sequence that involved the initial alkylation of racemic huprine Y, **2**, with 9-bromononanenitrile, followed by LiAlH$_4$ reduction of the resulting cyanoalkylhuprine **15** to the corresponding primary amine **16** [18], which was then coupled with 2-hydroxynicotinic acid or 3,5-dihydroxybenzoic acid, respectively, using *N*-ethyl-*N′*-(3-dimethylaminopropyl)carbodiimide hydrochloride (EDC·HCl), 1-hydroxybenzotriazole (HOBt), and Et$_3$N in a mixture EtOAc/DMF (Scheme 1). After silica gel column chromatography purification, carboxamides **9** and **11** were obtained in 45% overall yield.

Reaction of amine **16** with 1*H*-pyrazole-4-sulfonyl chloride in the presence of Et$_3$N in DMF afforded the target sulfonamide **10** in excellent yield (96%, 67% overall yield), after silica gel column chromatography purification (Scheme 1).

The hybrids **12** and **13** were synthetized in moderate yields by alkaline hydrolysis of cyanoalkylhuprine **15**, followed by acidification and EDC·HCl/HOBt-mediated amide coupling of the resulting carboxylic acid, in the form of quinoline hydrochloride salt, with 4-amino-1*H*-pyrazole or piperazin-2-one, respectively, and silica gel column chromatography purification (Scheme 2). Using the same reaction conditions, compound **17** was obtained in good yield from nitrile **15** and (2-methoxy-4-pyridyl)methanamine. Finally, treatment of the methoxypyridine derivative **17** with LiCl and *p*-toluenesulfonic acid monohydrate in DMF at 120 °C afforded the 2-pyridone analog **14** in moderate yield (Scheme 2).

All the target compounds **9**−**14** were transformed into the corresponding hydrochloride salts, by treatment with a methanolic solution of HCl, for their chemical characterization as well as *in vitro* and *in vivo* biological profiling. Due to the close structural similarity with **14**, its immediate precursor **17**, as the free base, was also subjected to biological evaluation.

2.3. In vitro and molecular modeling study of human BACE-1 inhibition

The new compounds were first profiled *in vitro* toward their primary targets, including BACE-1, AChE and BChE. The BACE-1 inhibitory activities of the novel hybrids and myricetin (IC$_{50}$ = 4.18 ± 0.50 μM) as a reference compound are collected in Table 1. Interestingly, hybrid **11** exhibited a potent hBACE-1 inhibitory activity (IC$_{50}$ = 2.71 μM) comparable to that of the lead rhein–huprine hybrid **1** (IC$_{50}$ = 1.50 μM) and myricetin, and compound **10** still displayed hBACE-1 inhibitory activity in the low micromolar

range (IC$_{50}$ = 10.8 μM, Table 1). In contrast, a low potency was found for compounds **9**, **12**, and **17** (7−26% hBACE-1 inhibition at an inhibitor concentration of 10 μM), while compounds **13** and **14** did not inhibit hBACE-1 at the tested concentration of 10 μM.

MD simulations were performed to gain insight into the features responsible for the BACE-1 inhibitory activity elicited by the most potent compounds, **10** and **11**, considering both enantiomeric forms of their huprine moiety. Accordingly, unbiased MD simulations (300 ns) were run for the complexes BACE-1–(7*R*,11*R*)-**10**, BACE-1–(7*S*,11*S*)-**10**, BACE-1–(7*R*,11*R*)-**11**, and BACE-1–(7*S*,11*S*)-**11** using Gromacs2018 (Fig. 4, see the Experimental Section for a detailed description of the computational protocol) [31]. Following our previous studies for the rhein–huprine hybrids [21], the huprine moiety was placed in the catalytic site of BACE-1, near the catalytic dyad formed by Asp32 and Asp228, and the nonamethylene linker of **1** was used as template to thread the tether of compounds **11** and **10** along the groove in order to enable the accommodation of the 3,5-dihydroxybenzamide or the pyrazole-4-sulfonamide moieties, respectively, in the cryptic pocket located at the edge of the groove, near Arg307, Asn233 and Phe322, which is occupied by the rhein unit in the complex of BACE-1 with **1**. Finally, the nonamethylene linker that connects the two subunits of **10** and **11** should confer a certain degree of flexibility to enable the expected dual site binding at the catalytic and secondary sites.

The hybrids (7*S*,11*S*)-**11** and (7*S*,11*S*)-**10** exhibited a stable binding to BACE-1, as confirmed by the small fluctuations in the positional root-mean-square deviation (RMSD) analysis of both the protein backbone and the ligand (Fig. 4; see also red profiles in Supplementary Fig. S2A–D). After the first 50 ns a conformational rearrangement occurred for the hybrid (7*R*,11*R*)-**11**, leading to a binding mode that remained stable till the end of the simulation, whereas a notable fluctuation that reflects a structural rearrangement of the ligand at the secondary binding site was observed at the end of the simulation run for (7*R*,11*R*)-**10**. These fluctuations primarily reflect structural rearrangements of the ligand at the secondary binding site. Thus, the two enantiomeric forms of the huprine unit were stably bound to the catalytic site of BACE-1, with the aminoquinoline unit filling the hydrophobic pocket formed by Leu 30, Tyr 71, Phe 108, Trp 115, and Ile 118 (Fig. 4). The protonated nitrogen of the aminoquinoline moiety was involved in a stable hydrogen-bonding interaction with the carboxyl group of Asp32 (average N⋯C (carboxylate) distance of 4 Å; black profiles in Supplementary Figs. S3A,B,D), and the flap loop (Pro 70–Ala 75), which contributes to shape the catalytic cleft of the enzyme, was stacked against the huprine moiety. The only exception was found for (7*S*,11*S*)-**11**, which was slightly displaced due to the deeper burial of the 3,5-dihydroxybenzamide moiety into the cryptic pocket, enabling close contacts with residues in the loop formed by residues 8−14. The shift of the huprine moiety caused the loss of the hydrogen-bonding interaction with Asp 32 (average N⋯C (carboxylate) distance of 8 Å; black profile in Supplementary Fig. S3C), which was replaced by a hydrogen bond with the hydroxyl moiety of Thr72 (average N⋯O distance of 3.5 Å; red profile in Supplementary Fig. S3C).

In contrast, the binding profile of the 3,5-dihydroxybenzamide and pyrazole-4-sulfonamide moieties of **11** and **10**, respectively, in the peripheral secondary site of BACE-1 was more variable. In the case of (7*R*,11*R*)-**11**, the two hydroxy groups of the 3,5-dihydroxybenzamide moiety (Fig. 4A) formed transient interactions with the backbone oxygen of Trp 262 (red profile in Supplementary Fig. S3A) and Phe 322 (green profile in Supplementary Fig. S3A), whereas a π–cation interaction was formed between the benzamide moiety of (7*S*,11*S*)-**11** and the guanidinium group of Arg 307 (average distance of 4.5 Å; green

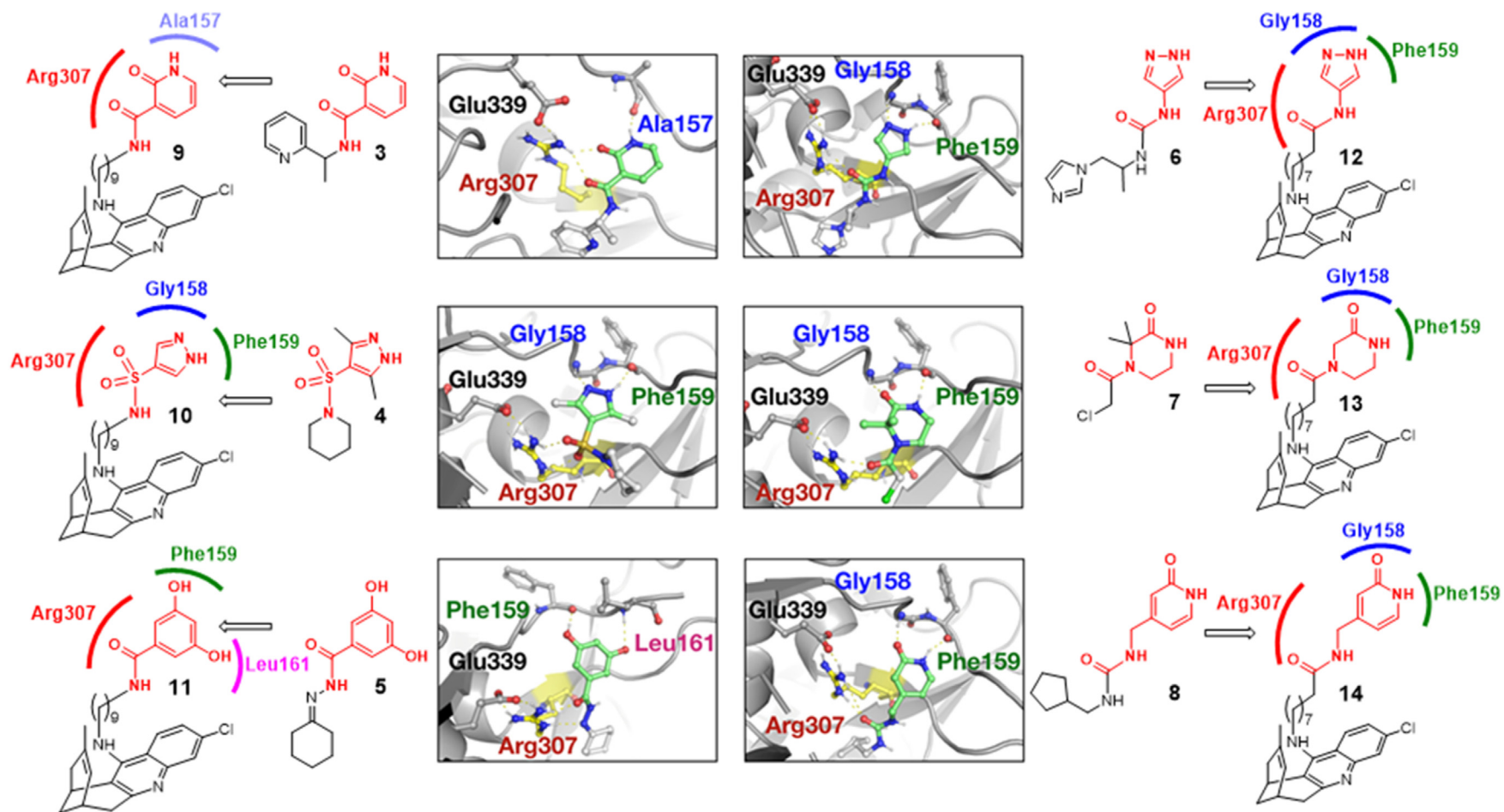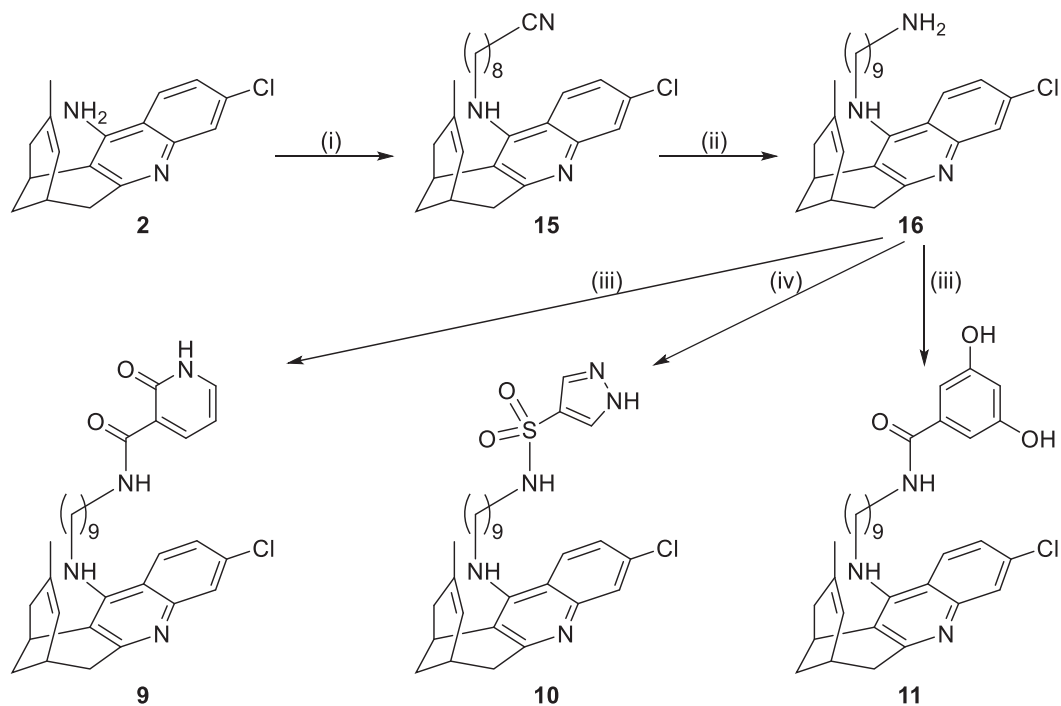**Fig. 3.** Structure of the identified BACE-1 secondary site virtual screening hits (VSH) **3**–**8** and design of the target compounds **9**–**14** from these VSH and huprine Y. The VSH-derived moieties incorporated in the hybrid compounds are highlighted in red.

Scheme 1. Synthesis of the target hybrids **9**−**11**. Reagents and conditions: (i) KOH, DMSO, rt, 2 h; then, 9-bromononanenitrile, rt, overnight, 73%; (ii) LiAlH₄, Et₂O, rt, overnight, 96%; (iii) 2-hydroxynicotinic acid (for **9**) or 3,5-dihydroxybenzoic acid (for **11**), EDC·HCl, HOBt, Et₃N, EtOAc/DMF, rt, 10 min; then, **16**, EtOAc/DMF, rt, overnight, **9** (64%), **11** (63%); (iv) 1*H*-pyrazole-4-sulfonyl chloride, Et₃N, DMF, rt, overnight, 96%.
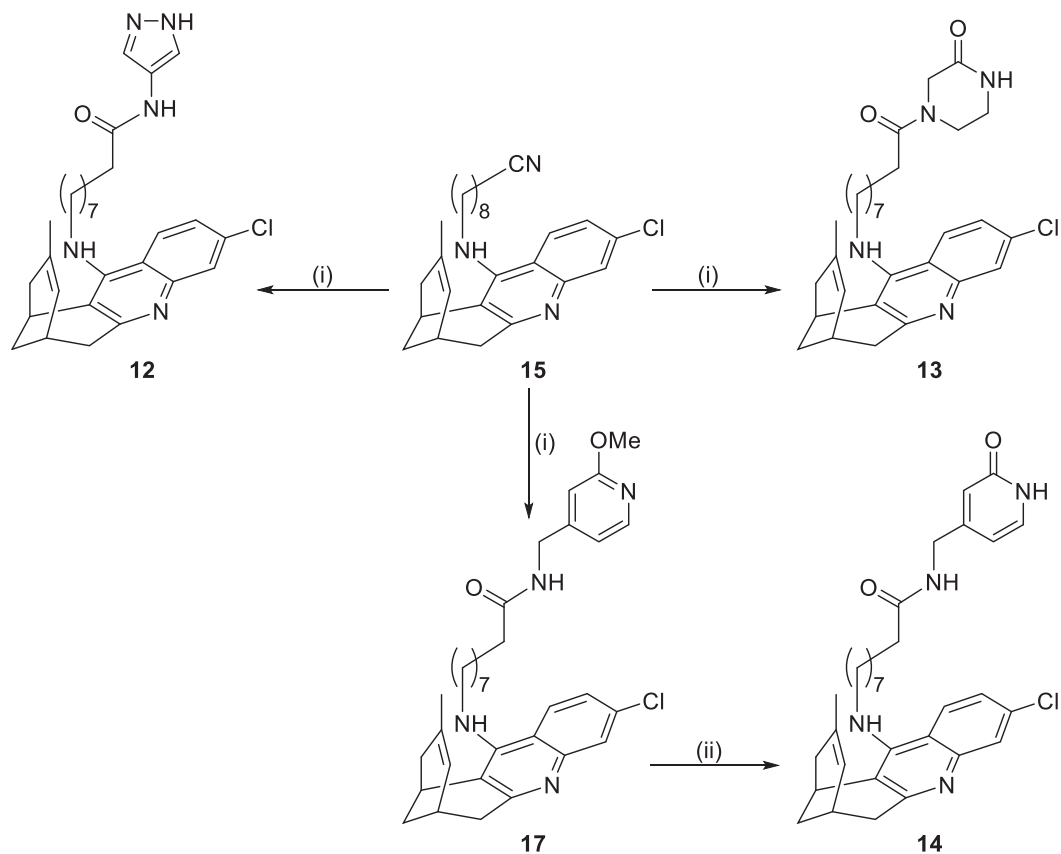
Scheme 2. Synthesis of the target hybrids **12**−**14**. Reagents and conditions: (i) 1) 40% methanolic KOH, reflux, 48 h; then, water, reflux, overnight; 5 N HCl; 2) crude carboxylic acid (quinoline hydrochloride salt), EDC·HCl, HOBt, Et₃N, EtOAc/DMF, rt, 10 min; then, 4-amino-1*H*-pyrazole (for **12**), piperazin-2-one (for **13**), or (2-methoxy-4-pyridyl)methanamine (for **17**), EtOAc/DMF, rt, overnight, **12** (47%), **13** (66%), **17** (74%); (ii) LiCl, *p*-toluenesulfonic acid monohydrate, DMF, 120 °C, 35 min, 54%.

Table 1
hBACE-1, hAChE, hBChE, Aβ42 and tau aggregation inhibitory activity of the target and reference compounds.

Compd	hBACE-1 IC$_{50}$ (μM) (or % inhib. @10 μM)[a]	hAChE IC$_{50}$ (nM)[b]	hBChE IC$_{50}$ (nM)[b]	Aβ42 aggregation in *E. coli* (% inhib. @10 μM)[c]	Tau protein aggregation in *E. coli* (% inhib. @10 μM)[c]
9	(6.92 ± 0.4)	1.82 ± 0.13	31.9 ± 1.4	42.3 ± 1.9	48.5 ± 2.3
10	10.8 ± 1.7	2.40 ± 0.25	50.3 ± 2.6	35.3 ± 2.8	55.5 ± 2.9
11	2.71 ± 0.2	2.57 ± 0.20	43.0 ± 2.7	49.5 ± 1.6	65.8 ± 1.9
12	(16.2 ± 0.4)	2.39 ± 0.84	64.0 ± 0.9	32.6 ± 2.5	45.3 ± 4.2
13	n.a.[d]	0.41 ± 0.04	74.8 ± 2.5	9.7 ± 3.5	15.0 ± 3.9
14	n.a.[d]	0.63 ± 0.09	75.8 ± 3.2	19.9 ± 4.2	20.9 ± 2.5
17	(26.5 ± 2.7)	1.25 ± 0.19	88.5 ± 5.4	29.4 ± 2.1	41.6 ± 2.9
1[e]	1.50 ± 0.38	3.60 ± 0.21	620 ± 20	47.9 ± 14.5	29.6 ± 8.5
2	(14 ± 0.1)[e,f]	1.07 ± 0.05[e]	181 ± 15[e]	8.9 ± 1.3[g]	7.6 ± 3.4[g]
myricetin	4.18 ± 0.50	nd[h]	nd[h]	nd[h]	nd[h]
donepezil	nd[h]	26.8 ± 6.5	6980 ± 540	nd[h]	nd[h]
propidium	nd[h]	nd[h]	nd[h]	39.2 ± 4.8	nd[h]
DP-128	nd[h]	nd[h]	nd[h]	68.2 ± 2.1	72.2 ± 2.1

[a] Concentration that leads to 50% inhibition of human recombinant BACE-1 activity or percentage inhibition of BACE-1 activity at 10 μM (% inhibition values between parentheses), with values being shown as mean ± standard deviation (SD) of 2 independent experiments (in triplicate).

[b] Concentration that leads to 50% inhibition of human recombinant AChE and human serum BChE activity, with values being shown as mean ± standard error of the mean (SEM) of at least 2 independent experiments (in triplicate).

[c] Percentage inhibition of the aggregation of Aβ42 and tau at a concentration of inhibitor of 10 μM in *E. coli* cells overexpressing these proteins, with values being shown as mean ± SEM of 9 independent experiments (in triplicate).

[d] Not active.

[e] Activities from Ref. [18], obtained with the same methodology.

[f] Percentage inhibition at a concentration of inhibitor of 5 μM.

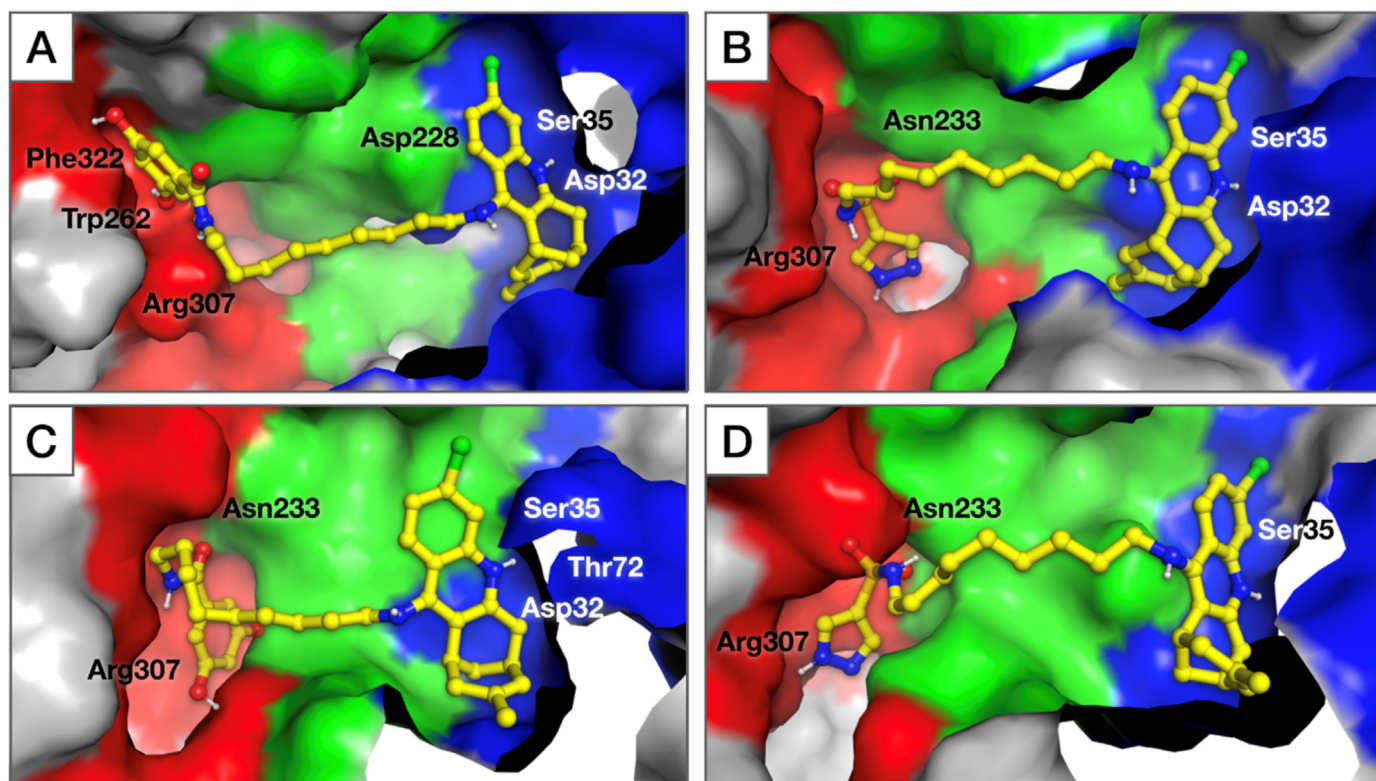[g] Activity from Ref. [30], obtained with the same methodology.

[h] Not determined.

Fig. 4. Representative structures of the BACE-1 complexes with (A) (7*R*,11*R*)-**11**, (B) (7*R*,11*R*)-**10**, (C) (7*S*,11*S*)-**11**, and (D) (7*S*,11*S*)-**10** derived from MD simulations performed using structural model of BACE-1 bound to the rhein–huprine hybrid **1** [21]. The catalytic site is highlighted in blue, the groove in green, and the secondary binding site in red. The location of selected residues is indicated with a white or black label, but representation of their side chains is omitted for the sake of clarity.

profile in Supplementary Fig. S3C), further assisted by hydrogen bonding with the backbone NH groups of Ser 11 and Gly 12. Regarding compound **10**, the pyrazole-4-sulfonamide of both enantiomers (Fig. 4B,D) forms stable hydrogen-bonding interactions with the side chain amide group of Asn 233 (red profile in Supplementary Fig. S3B; red, green and blue profiles in Supplementary Fig. S3D). Finally, the guanidinium group of Arg 307 remained stably placed relative to the pyrazole ring of the ligand (yellow profile in Supplementary Fig. S3D).

Compared with the rhein–huprine hybrid **1** examined in our previous studies [18,21], the rhein moiety adopted a tighter binding in the secondary binding site of BACE-1, where the hydrogen bond with Arg 307 was firmly maintained in MD simulations of (7*R*,11*R*)-**1** and (7*S*,11*S*)-1 (Supplementary Fig. S4). This may be ascribed to the larger size of rhein, which is deeply inserted into the binding pocket, as well as to the lower hydrophobicity of the 3,5-dihydroxybenzamide and pyrazole-4-sulfonamide moieties of the novel compounds **11** and **10** (clogP values of 0.4 and −0.7 for 3,5-dihydroxy-*N*-methylbenzamide and *N*-methyl-1*H*-pyrazole-4-sulfonamide versus 2.6 for the *N*-methylated rhein-carboxamide), which is reflected in a larger fraction of the polar surface area (40% and 57% for 3,5-dihydroxybenzamide or pyrazole-sulfonamide versus 37% for the amidated rhein). Although this explains the more labile binding of the 3,5-dihydroxybenzamide and pyrazole-4-sulfonamide moieties at the secondary binding site compared with the rhein scaffold, this also permits to increase the lipophilic efficiency of compounds **11** and **10** by 1.8 and 2.4 units (estimated by combining the pIC$_{50}$ data derived from Table 1 and logD values determined with ChemAxon) relative to the parent rhein–huprine compound **1** [32].

2.4. Inhibitory activity of human cholinesterases

In the central nervous system (CNS) the enzymes AChE and BChE operate jointly, but to a different extent depending on the disease stage, catalyzing the hydrolysis of the neurotransmitter acetylcholine (ACh), which aggravates the central cholinergic deficit and the cognitive impairment characteristic of AD patients. AChE plays a more preponderant role in the initial stages of AD, whereas BChE gains relevance as the disease progresses. Moreover, BChE inhibition has been linked to neuroprotective effects *in vitro* [33–35]. Thus, inhibition of AChE, BChE or both constitutes a well-established treatment option for AD, and the discovery of both selective and dual inhibitors of these cholinesterases is equally appealing for AD treatment [34–37].

A well-established colorimetric method [38] was used to assess *in vitro* the inhibitory potency of the target compounds on human recombinant AChE (hAChE) and human serum BChE (hBChE). The inhibitory activities are collected in Table 1, together with those of the rhein–huprine hybrid **1** and the parent huprine Y, **2**, for the sake of comparison. The activity of the anti-Alzheimer drug donepezil, as an additional reference compound, was also assessed.

A very high hAChE inhibitory potency was found for all the novel compounds, **9**−**14** and **17**. Indeed, these compounds displayed IC$_{50}$ values in the subnanomolar to low nanomolar range (IC$_{50}$ = 0.41−2.57 nM). Noteworthy, all of the hybrids were more potent hAChE inhibitors than the rhein–huprine hybrid **1** (up to 9-fold more potent) and more potent than donepezil (up to 65-fold), and four of them displayed a similar or even better potency than huprine Y (up to 2.6-fold more potent) (Table 1). Thus, the VSH-derived scaffolds of the hybrids **9**−**14** seem to contribute favorably to the binding to hAChE, more favorably than the much larger and lipophilic hydroxyanthraquinone moiety of the rhein–huprine hybrid **1**.

Likewise, compounds **9**−**14** and **17** were clearly superior to the reference compounds **1**, huprine Y, and donepezil regarding hBChE inhibition, with potencies 7−19-fold, 2−6-fold, and 79−219-fold higher, respectively (Table 1). Thus, the VSH-derived scaffolds of **9**−**14** seemed again to reinforce the binding to hBChE, leading to IC$_{50}$ values in the two-digit nanomolar range (IC$_{50}$ = 32−88 nM). Although these compounds are selective for hAChE over hBChE inhibition, they indeed display nanomolar potencies toward both enzymes, which, as mentioned above, is a favorable property for AD treatment.

2.5. Aβ42 and tau aggregation inhibition in Escherichia coli cells

Unlike the rhein–huprine hybrid **1**, the target compounds do not contain a hydroxyanthraquinone moiety, which was known to impart tau antiaggregating activity [15]. Notwithstanding this, we have consistently found that hybrids that are composed of two, preferably extended, π-systems connected by tether chains of suitable length display micromolar inhibitory activity toward the aggregation of tau, Aβ42 and other amyloidogenic proteins associated with neurologic disorders other than AD or with non-neurologic disorders [18,39–42]. Accordingly, we assessed the Aβ42 and tau anti-aggregating activity of the novel compounds **9**−**14** and **17** in a cell-based assay, which is based on the use of intact *Escherichia coli* cells that bear a plasmid to express either Aβ42 or tau and the measurement of the increase of fluorescence of the amyloid dye thioflavin S upon binding to aggregated Aβ42 or tau [43]. Active compounds internalize into the *E. coli* cells and inhibit the aggregation of the amyloidogenic protein, thereby preventing the increase of thioflavin S fluorescence. Table 1 collects the inhibitory activity of the new hybrids on the aggregation of Aβ42 and tau, measured as the percentage of inhibition of aggregation when using a concentration of inhibitor of 10 μM. For the sake of comparison, the anti-aggregating activities of the rhein–huprine hybrid **1** and huprine Y are also included in Table 1. The known Aβ42 anti-aggregating agent propidium iodide was also included as a reference compound (Table 1).

In agreement with our previous findings, compounds **9**−**12**, **14**, and **17**, bearing more or less extended aromatic VSH moieties, besides the huprine unit, exhibit both Aβ42 and tau anti-aggregating activity, with percentages of inhibition in the range 20−66% at 10 μM (Table 1). In contrast, compound **13**, featuring an aliphatic VSH moiety, is essentially inactive, like the parent compound huprine Y. Overall, the most potent compound is the 3,5-dihydroxybenzamido hybrid **11**, which inhibited Aβ42 and tau aggregation by 50% and 66%, respectively, at 10 μM, i.e., in a larger extent than the lead rhein–huprine hybrid **1** (48% and 30% inhibition, respectively) and huprine Y (9% and 8% inhibition, respectively), being slightly more potent or equipotent to the know Aβ42 anti-aggregating compound propidium iodide (39% inhibition at 10 μM) and slightly less potent that the reference compound DP-128 [39] (68% and 72% inhibition of Aβ42 and tau, respectively, at 10 μM).

2.6. Metal binding and antioxidant properties

While in healthy brain the levels of free metal ions are stringently regulated and kept at a low level, metal dyshomeostasis usually leads to disease states. Indeed, dyshomeostasis of redox-active biometals is a well-known pathogenic feature of AD and other neurodegenerative diseases [44,45]. High concentrations of metal ions such as Cu^{2+}, Zn^{2+}, and Fe^{2+} are found in Aβ plaques within the brains of AD patients, which potentiate Aβ aggregation and toxicity and contribute to the generation of oxidative stress, which is another crucial pathological event of AD, eventually leading to neuronal damage [46,47]. Thus, metal chelation, aimed at restoring biometal homeostasis, and antioxidant effects are further events of interest in the pursuit of disease-modifying drug candidates, and, as such, they have been considered in the design of multitarget anti-Alzheimer agents [48–50].

In light of the relevance of metal chelation for AD treatment and the presence of potentially chelating fragments within some of the VSH moieties of the hybrids, we screened for possible metal-binding effect of the compounds by incubating them with various metal ions, namely Cu^{2+}, Zn^{2+}, and Fe^{2+}. Changes in the UV−Vis spectra could indicate the formation of a complex. Especially

diazole compounds **10** and **12**, and the β-hydroxyamide derivative **9** showed a pronounced change in absorption after incubation with various metal ions (Supplementary Fig. S5), indicating possible metal-binding properties of these compounds. To follow this up, a pyrocatechol violet (PV) assay was performed according to Santos et al. with minor changes [51], using ethylenediaminetetraacetic acid (EDTA) as a reference compound for metal chelation (Fig. 5). Compounds with a shift in UV/Vis spectra after the addition of Cu^{2+} also showed a chelation effect in this assay (Fig. 5 and Supplementary Table S3). In particular, compounds **10** and **12** showed high Cu^{2+}-binding ability, similar to that of EDTA at compound/Cu^{2+} ratios of 5:1, 2:1, and 1:1, and even superior at a 0.5:1 ratio.

To investigate the potential intrinsic antioxidant effect of the novel compounds, they were subjected to the well-known 2,2-diphenyl-1-picrylhydrazyl (DPPH) free radical scavenging assay [52]. Compounds **12** and **14** displayed the best antioxidant activity, with EC_{50} values of 19.6 and 90.6 μM, respectively, whereas the rest of compounds showed only moderate or no antioxidant activity at the highest tested concentration (500 μM) (Supplementary Table S3). Of note, compound **12** exhibited an antioxidant effect similar to that of ascorbic acid (EC_{50} 11.8 μM), used as the reference antioxidant compound.

2.7. Neuroprotective effects

Among the new hybrids, compound **11** showed the best *in vitro* multitarget profile in terms of inhibition of hBACE-1, human cholinesterases, and Aβ42 and tau aggregation. This compound, together with hybrids **9**, **10**, and **12**, which exhibited the best metal chelating properties, were selected for further assessment of potential neuroprotective effects in HT22 mouse hippocampal neuronal cells. For this assay, concentrations of the target compounds up to 25 μM were used, as this concentration was found to be essentially nontoxic to this cell line (see below). Extracellular glutamate can be used to induce intracellular reactive oxygen species (ROS) accumulation in HT22 cells, which lack ionotropic glutamate receptors. This results in cell injury and eventually cell death [53]. To assess the neuroprotective effects of the new compounds, HT22 cells were challenged with 5 mM glutamate as a toxic insult or they were simultaneously incubated with the same concentration of the toxic insult plus different concentrations of the target compounds (1, 5, 10, or 25 μM) or quercetin (25 μM), as a positive control for neuroprotection. The well-established 3-(4,5-dimethylthiazol-2-yl)-2,5-diphenyl tetrazolium bromide (MTT) viability assay was then employed to assess the effects of the

different treatments on the viability of HT22 cells. Only compound **12** was found to protect HT22 cells against glutamate-induced neuronal death, exhibiting a dose-dependent effect that started at 10 μM and equaled that of quercetin at 25 μM (Fig. 6 and Supplementary Table S4).

2.8. Neurotoxicity

Since the novel compounds are to act in the CNS, it is important to assess their potential neurotoxicity. To this end, an MTT viability assay was performed with HT22 mouse hippocampal neuronal cell line. Most of the novel compounds were found to be non-neurotoxic at concentrations up to 25 μM (Fig. 7 and Supplementary Table S5), with only compound **10** exerting a low albeit significant toxicity at 10 μM.

2.9. Fish embryo acute toxicity (FET) test

Besides testing specific toxicities, like neurotoxicity, during the drug discovery process and before selecting a lead candidate, it is important to also screen for general toxicity in whole organism models. This step was classically performed in rodents, but nowadays the FET test is more and more used in the early preclinical phase because, according to the validated OECD guideline n.236 [54], it offers the potential to screen for acute toxicity, while reducing time, costs and the number of animals needed [55–57]. Thus, the FET test was conducted according to previously described conditions [58] to determine the lethal toxicity of the target hybrids on embryonic stages of zebrafish (*Danio rerio*). The test lasted for 72 h and every 24 h four indicators of lethality were evaluated according to the mentioned guideline: coagulation of eggs, lack of somite formation, lack of tail-bud detachment, and lack of heartbeat. At the end of the study lethality was determined based on a positive outcome in any of these four observations and the lowest observed adverse effect concentration (LOAEC) and lethal concentration killing 50% individuals (LC_{50}) were calculated.

Fertilized and synchronously divided zebrafish embryos were exposed to different concentrations of the novel compounds or the reference huprine Y, **2**, diluted in Danieau's solution (17.4 mM NaCl; 0.23 mM KCl; 0.12 mM $MgSO_4 \cdot 7H_2O$; 0.18 mM $Ca(NO_3)_2$; 1.5 mM HEPES; pH 7.4) and DMSO (1%) at rt for 72 h. For each compound a maximum concentration of 100 μM and four additional concentrations resulting from consecutive 1:2 dilutions were tested (100, 50, 25, 12.5, and 6.25 μM). Because compound **17** was producing more than 75% of lethality at concentrations from 12.5 to 100 μM, a dilution factor of 1:10 was applied in this case, so that it was tested
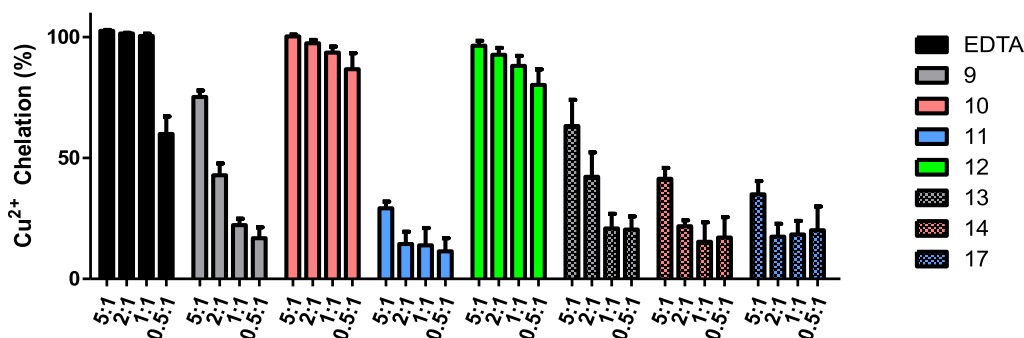

Fig. 5. Cu^{2+} chelation ability in the PV-assay, using sodium acetate buffer (50 mM, pH 6.0), $CuSO_4$ (300 μM) and different concentrations of the target compounds. Data are expressed as mean ± SD of three independent experiments, each performed in duplicate.
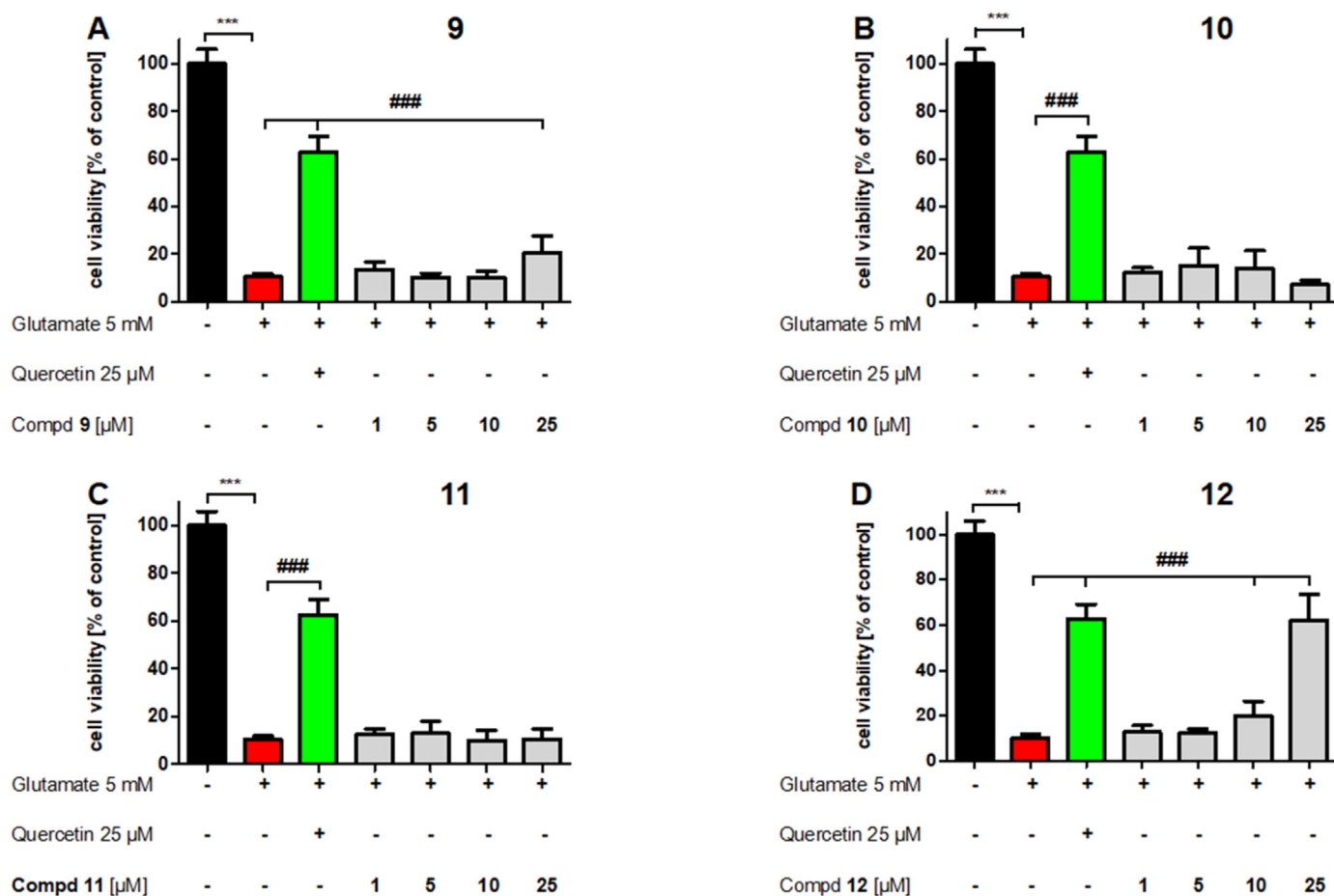
Fig. 6. Protective effect of compounds **9**–**12** against glutamate-induced oxidative stress in mouse hippocampal HT22 cells. The results are shown as mean ± SD of 3 independent experiments (in sextuplicate) and are referred to untreated control cells (100% cell viability). Data were analyzed by one-way ANOVA followed by Bonferroni multiple comparison post-test. The viability of HT22 cells treated with 5 mM glutamate was compared with that of untreated control cells (*), whereas the viability of HT22 treated with compounds **9**–**12** or quercetin was compared with that of the cells challenged 5 mM glutamate (#). *$p < 0.05$; **$p < 0.01$; ***$p < 0.001$; #$p < 0.05$; ##$p < 0.01$; ###$p < 0.001$.

at a maximum concentration of 10 μM. Under these assay conditions, all the compounds were found to be completely soluble at concentrations lower than the maximum tested concentration (MTC), i.e., in the range 10−50 μM, with the sole exception of compound **13**, which was soluble at 100 μM. Compounds **9**–**13** did not exert any significant lethality on zebrafish embryos at their maximum soluble concentrations (MSC, Table 2), and for compounds **10**, **11**, and **13** no significant lethality was observed at any of the tested concentrations (LOAEC >100 μM). However, compounds **14**, **17**, and the reference huprine Y produced a significant increase in lethality at 50, 10, and 25 μM concentrations, respectively. To compare the lethal potency among the compounds and with the reference huprine Y, LC$_{50}$ values were calculated and are given in Table 2, even if the calculated value is higher than the MSC. According to the LC$_{50}$ values, compound **17**, the synthetic precursor of **14**, was lethal to zebrafish embryos at relatively low concentrations (LC$_{50}$ = 7.1 μM), but gratifyingly all the target compounds were estimated to be safer than the reference compound huprine Y (LC$_{50}$ = 20.9 μM), with compounds **9** and **12** being moderately safer (LC$_{50}$ > 50 μM) and with **10**, **11**, **13**, and **14** being clearly safer (LC$_{50}$ > 100 μM, Table 2 and Fig. 8).

Overall, the target compounds **9**–**14** can be considered non-lethal after 72 h of exposure to whole embryos at concentrations well above those at which they exert their *in vitro* biological activities.

2.10. Blood–brain barrier penetration

To be effective, any drug purposed to act within the CNS must be able to penetrate across the BBB in sufficient amount to modulate its biological targets. To guarantee this requirement, the early stages of AD drug discovery programs usually include the preliminary determination of BBB permeability of the candidates. To this end, the so-called parallel artificial membrane permeability assay for BBB (PAMPA-BBB) [59] is commonly employed. This is a relatively easy-to-implement *in vitro* assay that models the permeation of the compounds by passive diffusion. By employing this assay, the BBB permeabilities (P_e) of the compounds **9**−**14** and **17** were assessed. The results are shown in Table 3, together with the permeabilities of the rhein–huprine hybrid **1** and huprine Y, for the sake of comparison. Interestingly, most compounds had permeabilities in the range 5.9×10^{-6} to 9.4×10^{-6} cm/s, i.e., over the value that indicated good brain penetration (5.2×10^{-6} cm/s, CNS+). Thus, the novel compounds should be expected to efficiently enter the brain. Of note, the permeability values of these compounds were lower than that of the lead rhein–huprine hybrid **1** (21.5×10^{-6} cm/s). This fact likely reflects a lower lipophilicity of the novel compounds relative to **1**, due to the polarity imparted by their VSH moiety.
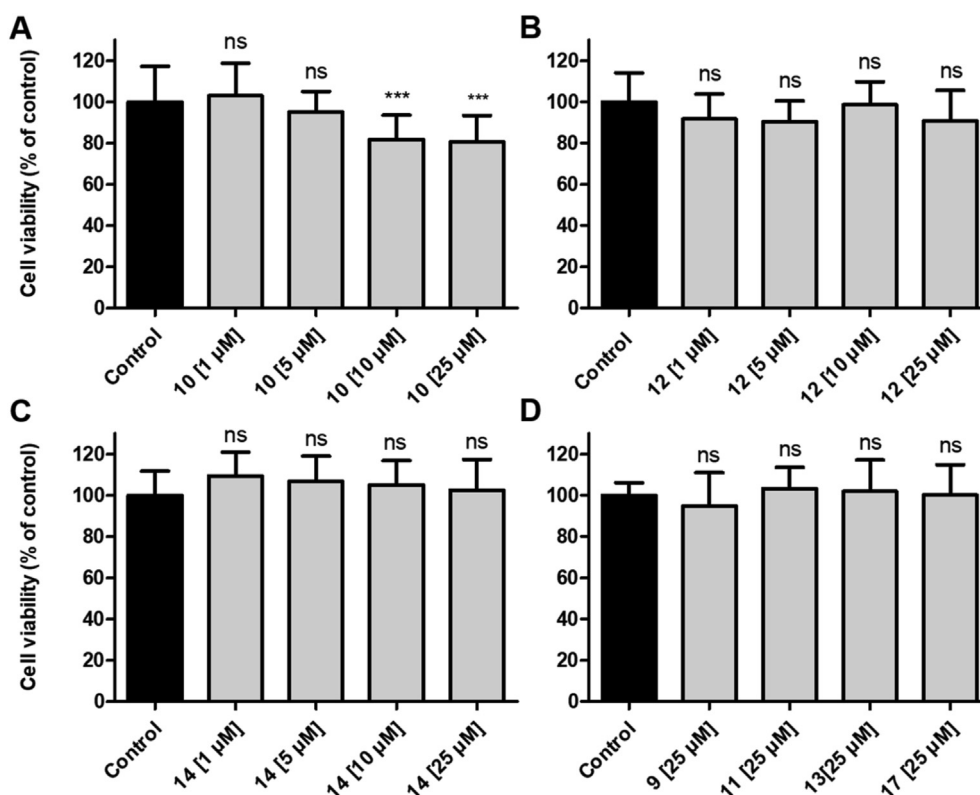
Fig. 7. Evaluation of the potential neurotoxicity of the target compounds on neuronal HT22 cells. Viability of HT22 cells treated with different concentrations (1, 5, 10, and 25 μM) of **10**, **12**, and **14** (A−C) or 25 μM of **9**, **11**, **13**, and **17** (D). Results are shown as mean ± SD of 3 independent experiments (in sextuplicate) and referred to untreated control cells (100% cell viability). Data were analyzed by one-way ANOVA followed by Bonferroni multiple comparison post-test. *$p < 0.05$; **$p < 0.01$; ***$p < 0.001$.

Table 2

Acute toxicity assessment of the target and reference compounds in zebrafish embryos.

Compd	Zebrafish embryo acute toxicity[a]			
	MTC (μM)	MSC (μM)	LOAEC (μM)	LC$_{50}$ (μM; CI$_{95}$)[b]
9	100	12.5	50	57.8 (45.5−77.6)
10	100	12.5	>100	>100
11	100	12.5	>100	>100
12	100	12.5	100	69.1 (56.9−84.5)
13	100	100	>100	>100
14	100	50	50	>100
17	10	10	10	7.1 (5.6−9.2)
2	100	25	25	20.9 (18.5−n.d.[c])

[a] Results of the zebrafish embryo acute toxicity assay indicating for each compound: the maximum tested concentration (MTC), maximum soluble concentration (MSC), lowest observed adverse effect concentration (LOAEC), and lethal concentration killing 50% individuals (LC$_{50}$). LOAEC and LC$_{50}$ were obtained from at least three independent experiments including 10 embryos per concentration and experiment, and five concentrations plus solvent control group (DMSO 1%) per experiment. LOAEC was calculated with ANOVA test and Bonferroni's post-hoc test for multiple comparison with a significance threshold established at $p < 0.05$, and is defined as the lowest concentration with significant adverse effects for lethality. LC$_{50}$ was calculated by adjusting the results of the means of the six tested groups of at least three experiments per compound to a non-linear concentration–response curve with variable slope and least squares fit with minimum and maximum fixed values at 0 and 100% of lethality.

[b] CI$_{95}$: confidence interval for LC$_{50}$.

[c] n.d.: Not possible to be determined by the statistical model due to too wide range.

2.11. Aqueous solubility

Solubility is an important physicochemical property to consider in drug discovery, as it determines the ability of a drug to be absorbed, and, hence, its oral bioavailability [60]. In drug discovery, kinetic solubility is measured by fully dissolving the compounds in an organic solvent, usually DMSO, and then diluting with an aqueous buffer, such as phosphate buffered saline (PBS). We measured the kinetic solubility of all the target compounds and that of **1**, for comparison. Assay validation was carried out by measuring the solubility of two marketed drugs (prazosin and progesterone) and comparing the obtained solubility values (61.2 and 2.6 μM, respectively) with those reported in the literature (26.3 and 3.7 μM, respectively) [61]. The solubility of the novel compounds is in the range of 9.0−77.4 μM (or 5.1−43.3 μg/mL) (Table 3). Three of the novel compounds, i.e., **11**, **12** and **14** have solubilities similar to that of the rhein−huprine hybrid **1** (19.7 μM) and one of them, **13**, has a much higher solubility (77.4 μM). Overall, compounds **11**, **13** and **14**, as well as **1**, with solubilities of 10.8, 43.3, 13.8 and 14.8 μg/mL, respectively, can be considered of moderate solubility, according to solubility classification ranges suggested for medicinal chemists, which consider a range of 10−60 μg/mL for this category [60].

2.12. In vivo efficacy studies in SAMP8 mice

After the *in vitro* profiling of the multiple activities, toxicity, and brain permeability of all the target hybrids, compound **11** stood out as the most potent towards BACE-1 and Aβ42 and tau aggregation, with dual nanomolar hAChE and hBChE inhibitory activity, lack of toxicity in hippocampal neuronal HT22 cells and in zebrafish embryos at concentrations of 25 and 100 μM, respectively, ability to enter into the brain and moderate aqueous solubility. To further confirm **11** as an anti-Alzheimer lead, an *in vivo* proof-of-concept in senescence-accelerated mouse prone 8 (SAMP8) mice was performed. SAMP8 mice are considered an animal model of late-onset
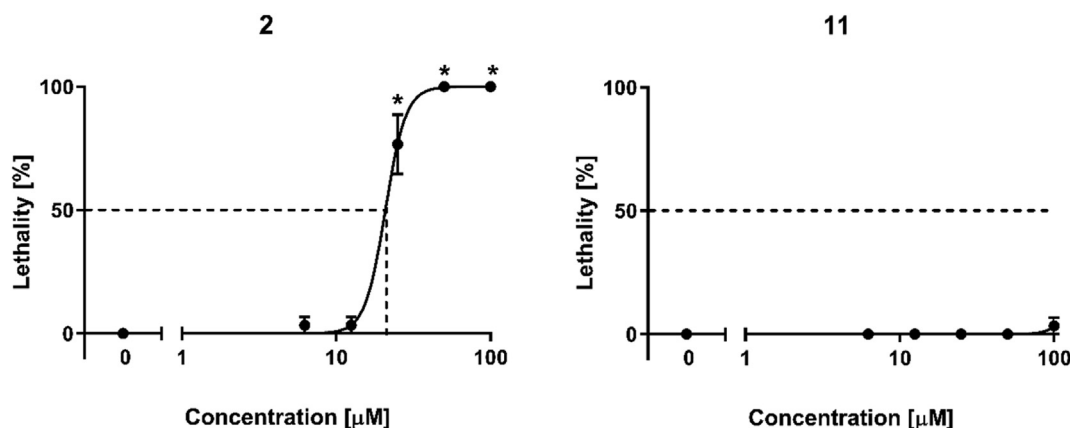
Fig. 8. Lethality of zebrafish embryos exposed to the reference compound **2** or the target hybrid **11** at concentrations from 1 to 100 μM. Results are presented as mean ± SEM of at least three independent experiments with 10 embryos per concentration in each experiment (in total at least 30 embryos per concentration). *$p < 0.05$ by one-way ANOVA and Bonferroni's post-hoc test for multiple comparisons. LC_{50} calculated by adjusting the results of the means and SEMs to a non-linear concentration–response curve with variable slope and least squares fit with minimum and maximum fixed values at 0 and 100% of lethality.

Table 3
PAMPA-BBB permeability and aqueous solubility of the target compounds.

Compd	Brain permeability Pe $(10^{-6}$ cm/s)[a]	Aqueous solubility	
		μM	μg/mL
9	6.7 ± 0.4 (CNS+)	12.4	7.7
10	6.3 ± 0.3 (CNS+)	9.0	5.7
11	9.4 ± 0.2 (CNS+)	18.1	10.8
12	5.9 ± 0.4 (CNS+)	16.0	9.3
13	4.9 ± 0.6[b] (CNS±)	77.4	43.3
14	4.4 ± 0.1[b] (CNS±)	23.7	13.8
17	8.2 ± 0.1 (CNS+)	9.0	5.1
1	21.5 ± 0.7[c] (CNS+)	19.7	14.8

[a] *In vitro* brain permeability as measured in the PAMPA-BBB assay, with values being expressed as the mean ± SD of 3 independent experiments (in triplicate). High BBB permeation (CNS+) when $P_e > 5.2 \times 10^{-6}$ cm/s; low BBB permeation (CNS−) when $P_e < 1.9 \times 10^{-6}$ cm/s; uncertain BBB permeation (CNS±) when 5.2×10^{-6} cm/s > $P_e > 1.9 \times 10^{-6}$ cm/s.
[b] Poor dissolution was observed.
[c] Data from Ref. [18], obtained with the same methodology.

AD, which develops an accelerated process of senescence, recapitulating several AD hallmarks, such as altered APP processing, tau hyperphosphorylation, oxidative stress, neuroinflammation, and age-related cognitive decline [62–67]. For this mouse model, the so-called senescence-accelerated mouse resistant 1 (SAMR1) strain is considered the same genetic background healthy control mice.

Seven-month-old male SAMP8 mice were treated chronically with **11** at a dose of 2 mg/kg/day (oral administration) during 4 weeks and then subjected to behavioral evaluation and molecular analyses. For comparison, two parallel groups of vehicle-treated SAMP8 and SAMR1 control mice were included in the study. Neither mortality nor toxic effects were observed in the animals along the treatment period, which confirmed a favorable safety and tolerability profile of **11** at the studied dose.

2.12.1. Behavioral tests

At the end of the treatment, two different behavioral and cognitive tests were performed to study the effects of compound **11** on working and spatial memory. A modification of the novel object recognition test (NORT) protocol was performed [68]. In brief, mice were habituated to a 90° two-arm (25 × 20 × 5 cm) black maze for 10 min during 3 consecutive days. On day 4, the animals were subjected to a 10 min acquisition trial, in which they were allowed to freely explore two identical objects located at the end of each arm (first trial-familiarization). After 2 h (for short-term memory evaluation) and 24 h (for long-term memory evaluation) from the first trial, the mice were subjected to a 10 min retention trial, in which one of the two identical objects had been replaced by a novel one. The behavior was recorded, the times spent by the mice exploring the new object (TN) and the old one (TO) were measured manually, and a discrimination index (DI) was calculated as (TN − TO)/(TN + TO).

Vehicle-treated SAMP8 mice exhibited severe cognitive impairment relative to vehicle-treated SAMR1 mice, which led to an essentially null discrimination index in both short- and long-term tests (Fig. 9A). Treatment with **11** clearly rescued SAMP8 mice from their working memory impairment, as evidenced by a fully recovered discrimination index, which reached the levels of the control strain SAMR1 (Fig. 9A). Thus, short- and long-term memories were significantly improved in SAMP8 mice upon chronic treatment with **11**, indicating a positive effect of this compound on working memory.

To further explore the effects of compound **11** on cognitive abilities, an object location test (OLT) was performed to assess its effect on spatial memory. The OLT is a well-established task based on the spontaneous tendency of rodents to recognize when an object has been relocated, which makes the mice to spend more time exploring the novel location of the object than the familiar location [65]. The test was carried out in three days in a wooden box (50 × 50 × 25 cm) with three white walls and one black wall. The first day, the box was empty, and the animals were habituated to the open field arena for 10 min. The second day, two identical objects were placed in front of the black wall, equidistant from each other and the wall, and the animals were placed into the open field arena and allowed to explore both objects and surroundings for 10 min. The third day, one object was moved from its original location and was placed in front of the white wall. The behavior of the mice was recorded, the times spent sniffing the object in the new (TN) and old (TO) location (TN) were measured, and the DI was calculated as (TN − TO)/(TN + TO) to assess the cognitive performance.

Like in the NORT tests, we observed an absolute lack of discrimination in vehicle-treated SAMP8 mice compared with the control strain SAMR1, which is indicative of a severe spatial memory impairment (Fig. 9B). Very interestingly, treatment of SAMP8 mice with **11** led again to a total recovery of the discrimination index, which reached the levels found in control SAMR1 mice, thereby demonstrating a rescuing effect of **11** on spatial memory.
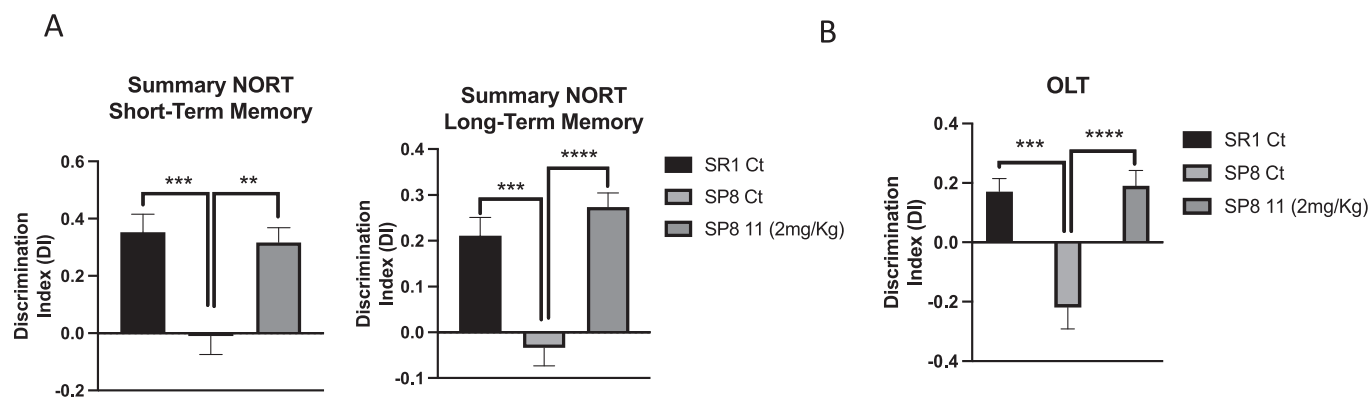
A

B

Fig. 9. Results of NORT for short-term and long-term memory (A) and OLT (B) in 7-month-old male SAMP8 (SP8) and SAMR1 (SR1) mice. Values of the discrimination index (DI) are represented as mean ± SEM; n = 30 (SR1 control (Ct) n = 10, SP8 Ct n = 10, and SP8 treated with **11** (2 mg/kg, SP8 11, n = 10). Data were analyzed by one-way ANOVA followed by Tukey post-hoc test. $**p < 0.01$; $***p < 0.001$; $****p < 0.0001$.

Overall, these two behavioral studies demonstrated a very clear cognition-enhancing effect of compound **11** in this mouse model of late-onset AD.

2.12.2. Effects on amyloid processing pathway and tau pathology

The potent anticholinesterase activity of compound **11**, which should lead to an increased cholinergic neurotransmission in the CNS, might in part account for its beneficial effects on cognition. Besides this, the improved cognition of SAMP8 mice treated with **11** might also arise from disease-modifying effects generated from other activities elicited by this compound, such as BACE-1 inhibition. To this end, we first examined the effects of **11** on the amyloid pathology in SAMP8 mice. APP can be processed through two mutually exclusive pathways that are mediated by an initial cleavage by either α-secretase (non-amyloidogenic pathway) or β-secretase (amyloidogenic pathway) followed by a second cleavage by γ-secretase. α-Secretase cleaves APP within the Aβ sequence, thereby precluding the final formation of Aβ. In particular, the α-secretase activity, mediated by enzymes from the family of a disintegrin and metalloproteinases (ADAMs), such as ADAM10, gives rise to an initial amino-terminal fragment called secreted APPα (sAPPα) and the carboxy-terminal fragment CTF83, which undergoes subsequent cleavage by γ-secretase affording non-amyloidogenic peptides, namely p3 and an amino-terminal APP intracellular domain (AICD). In contrast, cleavage of APP by β-secretases, such as BACE-1, the major β-secretase in the brain, leads to secreted APPβ (sAPPβ) and CTF99, which is later transformed into Aβ by γ-secretase [69].

BACE-1 inhibition should result in reduced levels of the APP fragments resulting from the β-secretase pathway, such as sAPPβ, and an increase of the alternative APP processing by the α-secretase pathway, with formation of the corresponding APP fragments, such as sAPPα. Very gratifyingly, consistently with the BACE-1 inhibitory activity of **11**, SAMP8 mice chronically treated with this compound had significantly reduced levels of sAPPβ and significantly increased levels of sAPPα in the hippocampus as compared with control mice (Fig. 10A and B).

Beyond the putative direct effect of **11** on the amyloid pathology by BACE-1 inhibition, we found that treatment of SAMP8 mice with this compound led to increased gene expression of *Adam10*, the α-secretase responsible for sAPPα release from APP, and to a significant decrease in the gene expression of *Bace1*, the β-secretase involved in the cleavage of APP to sAPPβ (Fig. 10C). We next explored the potential effects of compound **11** on the enzymatic machinery to remove amyloid species, by measuring the gene expression of *insulin-degrading enzyme* (*Ide*) and *neprilysin* (*Nep*),

two of the most prominent amyloid degrading enzymes [70,71]. Treatment of SAMP8 mice with **11** did not alter the gene expression of *Ide* but led to a tendency towards increased levels of *Nep*, even though this change did not reach statistical significance (Fig. 10D). Thus, chronic treatment of SAMP8 mice with **11** ameliorated amyloid pathology by shifting APP processing towards the α-secretase non-amyloidogenic pathway and increasing Aβ clearance.

Tau hyperphosphorylation is a marker of neurodegeneration in AD and other degenerative pathologies [72]. Compound **11** was able to modify the activation of glycogen synthase kinase 3β (GSK3β), one of the main enzymes involved in tau phosphorylation, by increasing the protein levels of the phosphorylated enzyme (pGSK3β; Ser 9), the inactive form of the kinase, which should lead to diminished tau phosphorylation (Fig. 10E). Indeed, SAMP8 mice treated with compound **11** showed significantly reduced levels of tau hyperphosphorylation at epitope Ser 404 (Fig. 10F), thereby confirming a beneficial effect of this compound on tau pathology.

2.12.3. Modulation of oxidative stress and neuroinflammation

In neurodegeneration, particularly in AD, there exists a misbalance in inflammation and oxidative stress [73,74]. To study the effect of compound **11** on these pathologies, changes in oxidative stress markers and gene expression of cytokines, as a measure of the inflammatory response, were determined in SAMP8 mice after chronic treatment with **11**. Expression levels of the antioxidant gene *heme oxygenase 1* (*Hmox1*) were slightly increased ($p < 0.0634$) in treated mice compared to control animals, whereas no changes were found for the gene expression levels of *cyclooxygenase 2* (*Cox-2*), an enzyme related to increased oxidative stress (Fig. 11A). Therefore, the analysis of these two markers indicated that compound **11** did not elicit any specific effect on the modulation of oxidative stress.

To assess the effect of **11** on neuroinflammation, the gene expression of different inflammatory mediators was assessed in the hippocampus of SAMP8 mice. It is known that SAMP8 mice show an increased inflammatory response [75]. Accordingly, significant increase or tendency to increase were found in the gene expression levels of the proinflammatory mediators *interleukin 1β* (*Il-1β*), *interleukin 6* (*Il-6*), and *tumor necrosis factor α (Tnf-α)* in control SAMP8 mice in comparison with SAMR1 mice (Fig. 11B). By contrast, no changes between strains were observed for *C-X-C motif chemokine ligand 10 (Cxcl10)* and *interferon-γ (Ifn-γ)*. Compound **11** treatment led to a reduced gene expression of *Il-1β*, *Il-6*, *Cxcl10*, and *Tnf-α*, even though this effect did not reach statistical significance (Fig. 11B).
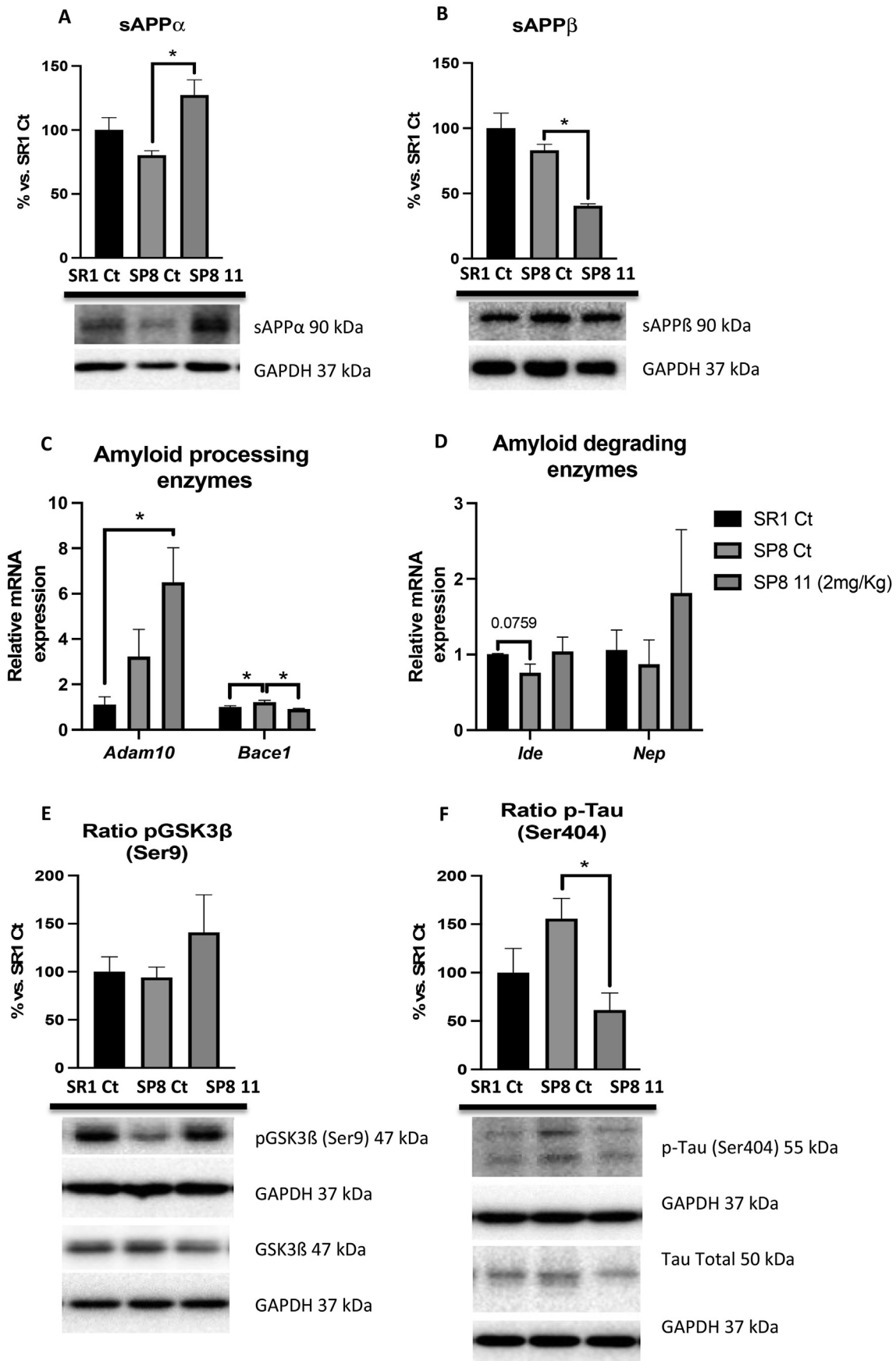
Fig. 10. Quantification and representative Western Blot analysis of sAPPα (A), sAPPβ (B), ratio pGSK3β (E), and ratio p-Tau (Ser404) (F) from hippocampal tissue of 7-month-old male SAMP8 (SP8) and SAMR1 (SR1) mice. Values in bar graphs are adjusted to 100% for protein levels of the SR1 Control. Values are the mean ± SEM; n = 3 for each group. Gene expression of amyloid processing enzymes *Adam10* and *Bace1* (C), as well as amyloid degrading enzymes *Ide* and *Nep* (D). Gene expression levels were determined by real-time PCR. Values represented are mean ± SEM; n = 12 (SR1 control (Ct) n = 4, SP8 Ct n = 4, and SP8 treated with **11** (2 mg/kg, SP8 11, n = 4). Data were analyzed by one-way ANOVA followed by Tukey post-hoc test. $*p < 0.05$.

14

2.12.4. Effects on synaptic protein levels

To further explore potential disease-modifying effects resulting from the chronic treatment with **11**, we measured the hippocampal levels of two synaptic proteins, i.e., postsynaptic density protein 95 (PSD95) and synaptophysin (SYN). PSD95 is a key scaffold protein that regulates the trafficking and localization of glutamate receptors in excitatory neurons, with an essential role in synaptic plasticity [76], whereas SYN is the most abundant synaptic vesicle protein [77]. A significant increase of PSD95 levels and a clear tendency towards increased SYN levels was found in SAMP8 mice chronically treated with **11** (Fig. 12) compared with vehicle-treated control mice, thereby confirming a beneficial effect of this compound on synaptic plasticity, which might be behind the cognitive improvement observed in the behavioral tests.

Taken together, the results achieved in the chronic efficacy studies in SAMP8 mice demonstrate the neuroprotective and therapeutic potential of **11**, which ameliorates several key underlying mechanisms of AD, including amyloid processing, tau hyperphosphorylation, and neuroinflammation, leading to improved synaptic plasticity and cognition.

3. Conclusion

Simultaneous occupancy of the catalytic site and a floppy secondary site of BACE-1 by the aminoquinoline and hydroxyanthraquinone moieties of the multitarget rhein–huprine hybrid **1** seems to account for its high inhibitory potency towards this enzyme. With the aim of developing new multitarget anti-Alzheimer agents that retain the dual-site binding to BACE-1 of compound **1** while bearing smaller and less lipophilic secondary site interacting motifs, we have performed a virtual screening campaign directed to this secondary binding site of BACE-1. This has led to the identification of six potential hits, whose scaffolds have been combined with the huprine moiety and a linker equivalent to that of **1**. Four out of the six synthesized hybrids turned out to be weak BACE-1 inhibitors or inactive. Indeed, BACE-1 is considered a target of difficult ligandability through small molecules [25,78]. Fortunately, according to our expectations, two hybrids (**10** and **11**) displayed BACE-1 inhibitory activity, with the 3,5-dihydroxybenzamido-substituted hybrid **11** exhibiting a similar potency to that of compound **1**, under the same assay conditions. This finding was in agreement with the structural stability observed in the MD simulations run for the complex formed by **11** bound to BACE-1, where the huprine moiety was tightly bound to the catalytic pocket whereas the 3,5-dihydroxybenzamido unit filled the floppy secondary site located at the end of the groove.

Additionally, all the new hybrids outperformed both compound **1** and the parent huprine Y as dual inhibitors of hAChE and hBChE, with IC_{50} values in the subnanomolar to nanomolar range for both enzymes, which suggests that the VSH scaffolds of these hybrids contribute positively to the interaction with both cholinesterases, and some of them, especially **11**, were also superior to **1** and huprine Y as dual inhibitors of Aβ42 and tau aggregation. This combined biological profile was enriched in some compounds with biometal chelating and antioxidant properties. Finally, most of the compounds exhibited in vitro PAMPA-BBB permeability above the threshold for good brain penetration and were found to be nontoxic both in a model of neurotoxicity in mouse hippocampal neuronal HT22 cells (up to 25 μM) and in a model of acute toxicity in zebrafish embryos (up to 50−100 μM), at concentrations well above those at which they display their different in vitro activities.

Chronic in vivo efficacy studies on compound **11** (2 mg/kg/day, oral administration, 4 weeks) in SAMP8 mice, a mouse model of late-onset AD that features accelerated aging with severe memory and learning impairment, have shown that it completely restores short- and long-term working and spatial memory of treated SAMP8 mice. Moreover, treatment with compound **11** led to significantly decreased levels of sAPPβ and increased levels of sAPPα in hippocampus, which likely arise from its BACE-1 inhibitory activity. Very interestingly, beyond this putative effect on BACE-1, treatment of SAMP8 mice with **11** led to significantly increased hippocampal gene expression levels of *Adam10* (α-secretase) and decreased levels of *Bace1* (β-secretase). Thus, treatment of SAMP8 mice with compound **11** led to an overall shift of APP processing towards the non-amyloidogenic α-secretase pathway, to the detriment of the amyloidogenic β-secretase pathway. As an additional beneficial in vivo effect of **11** regarding the amyloid pathology, this compound produced a tendency towards increased levels of the amyloid degrading enzyme neprilysin. Thus, oral treatment of SAMP8 mice with compound **11** ameliorated amyloid pathology, reducing the formation of Aβ and increasing its degradation and clearance. The disease-modifying effects of **11** also reached tau and oxidative stress pathologies, neuroinflammation, and synaptic dysfunction. Thus, SAMP8 treated mice showed significantly reduced hippocampal levels of phosphorylated tau at Ser 404 residues and a positive tendency towards increased gene expression levels of the antioxidant enzyme *Hmox1*, reduced gene expression levels of proinflammatory cytokines *Il-1β*, *Il-6*, *Cxcl10*, and *Tnf-α*, and increased levels of the synaptic proteins PSD95 and SYN. Overall, the BACE-1-directed virtual screening-derived compound **11** constitutes a promising new anti-AD lead able to positively impact memory and learning and interfere with the natural course of AD-like pathology at multiple levels.

4. Experimental section

4.1. Virtual screening for ligands of the cryptic binding site of BACE-1

A library of ~500.000 commercially available fragment-like/small compounds (molecular weight between 150 and 300) was downloaded from the ZINC12 database [79]. All the compounds were prepared using the LigPrep module of Maestro (Schrödinger suite) [80] in order to generate the 3D structures. A preliminary screening was performed to select those compounds able to satisfy a pharmacophore model consisting of i) two hydrogen bond acceptor sites separated by 2.8 Å and located close to Arg 307, and ii) a hydrogen bond donor located close to the carboxylate group of Glu 310. Let us note that these pharmacophore constraints were chosen to mimic anchoring points observed for the rhein moiety in previous MD simulations performed for the rhein−huprine hybrid **1** [21]. In particular it was observed that the carbonyl group of the hydroxyanthraquinone moiety of rhein formed a hydrogen bond with the guanidinium moiety of Arg 307, whereas the edge of the rhein moiety opposite to Arg 307 formed electrostatic contacts with Glu 310. The subset of compounds that satisfied at least two of these constraints (283,130) were then virtually screened over two selected BACE-1 structures/models derived from previous MD simulations [21], which are characterized by the presence of an open secondary binding site and mainly differ in the orientation adopted by the key residue Arg 307. In model 1, the Nε of the guanidine moiety is oriented towards the interior of the protein and forms a hydrogen-bonding interaction with the backbone carbonyl moiety of Gln 304, whereas in model 2 the Nε is pointing to the solvent environment. A virtual screening workflow was performed by combining a preliminary high-throughput virtual screening (HTVS) followed by a second screening with the Extra Precision (XP) docking algorithm implemented in Glide [81].
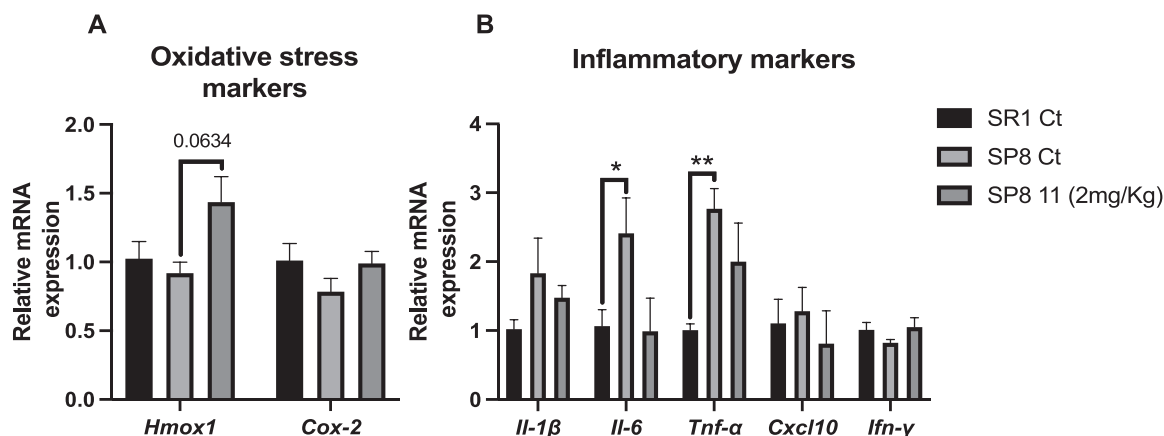
A Oxidative stress markers

B Inflammatory markers

SR1 Ct
SP8 Ct
SP8 11 (2mg/Kg)

Fig. 11. Gene expression of oxidative stress markers *Hmox1* and *Cox-2* (A) as well as inflammatory markers *Il1-β, Il-6, Tnf-α, Cxcl10*, and *Ifn-γ* (B) in hippocampal tissue of 7-month-old male SAMP8 (SP8) and SAMR1 (SR1) mice. Gene expression levels were determined by real-time PCR. Values are shown as mean ± SEM; n = 12 (SR1 control (Ct) n = 4, SP8 Ct n = 4, and treated with **11** (2 mg/kg, SP8 11, n = 4)). Data were analyzed by one-way ANOVA followed by Tukey post-hoc test. *$p < 0.05$; **$p < 0.01$.
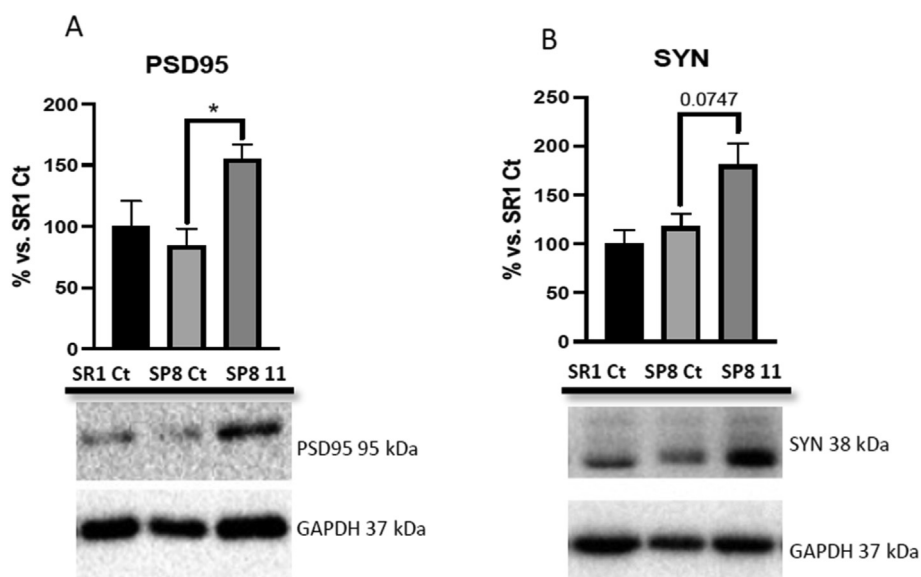
A PSD95

B SYN

Fig. 12. Quantifications and representative Western Blot for PSD95 (A) and SYN (B) from hippocampal tissue of 7-month-old male SAMP8 (SP8) and SAMR1 (SR1) mice. Values in bar graphs are adjusted to 100% for protein levels of the SR1 control. Values are the mean ± SEM; n = 3 for each group. Data were analyzed by one-way ANOVA followed by Tukey post-hoc test. *$p < 0.05$.

4.2. Chemistry

4.2.1. General procedures

All reagents and solvents were purchased from commercial suppliers (Merck, Acros, Cymit) unless otherwise stated, and used without further purification. The progress of the reactions was monitored by thin-layer chromatography (TLC) using aluminum-backed sheets with silica gel 60 F254 (Merck, ref 1.05554), using CH_2Cl_2/MeOH/50% aq NH_4OH mixtures as solvent system. The spots were visualized by UV irradiation and/or 1% aq. $KMnO_4$, followed by charring with a heat-gun. Column chromatography was performed on silica gel 60 AC.C (35−70 mesh, Carlo Erba, ref 2000027). Melting points were determined in open capillary tubes with an MFB 595010 M Gallenkamp melting point apparatus. IR spectra were run on a PerkinElmer Spectrum RX I spectrophotometer. Absorption values are expressed as wavenumbers (cm^{-1}); only significant absorption bands are given. 400 MHz ^{1}H/100.6 MHz ^{13}C NMR spectra were recorded on a Varian Mercury 400 spectrometer,

at the Centres Científics i Tecnològics of the University of Barcelona (CCiTUB). The chemical shifts are reported in ppm (δ scale) relative to solvent signals (CD_3OD at 3.31 and 49.0 ppm in the ^{1}H and ^{13}C NMR spectra, respectively), and coupling constants are reported in Hertz (Hz). Assignments given for the NMR spectra of the new compounds have been carried out on the basis of COSY ^{1}H/^{1}H (standard procedures) and COSY ^{1}H/^{13}C (gHSQC and gHMBC sequences) experiments. The *syn (anti)* notation of the protons at position 13 of the huprine moiety of the target hybrids means that they are on the same (different) side of the quinoline moiety with respect to the cyclohexene ring. High-resolution mass spectra were carried out at the CCiTUB with a LC/MSD TOF Agilent Technologies spectrometer. Analytical RP-HPLC was performed with an Agilent 1260 Infinity II HPLC system coupled to a photodiode array, using a Poroshell 120 EC-C18 (50 × 4.6 mm, 2.7 μm) column at 40 °C, with a mobile phase consisting of mixtures of A (0.05% formic acid in water) and B (0.05% formic acid in acetonitrile) (gradient A/B 95:5, 3 min; B, 4 min; A/B 5/95 1 min), a flow rate of 0.6 mL/min, and

$\lambda = 254$ nm as detection wavelength (for compounds **9**–**11**, **14**, and **17**) or with an Agilent 1100 Series HPLC system equipped with an UV detector 1315A, using a Kromasil 100C18 (250×4.6 mm, 10 μm) column, acetonitrile/H_2O mixtures containing 0.1% Et_3N (gradient from 51% to 85% to 51% acetonitrile in 30 min) as the eluent, a flow rate of 1 mL/min, and $\lambda = 220$ nm as detection wavelength (for compounds **12** and **13**). The analytical samples of all of the compounds that were subjected to pharmacological evaluation possessed a purity ≥95% as evidenced by HPLC measurements.

4.2.2. N-{9-[(3-Chloro-6,7,10,11-tetrahydro-9-methyl-7,11-methanocycloocta[b]quinolin-12-yl)amino]nonyl}-2-oxo-1,2-dihydropyridine-3-carboxamide (9)

To a suspension of 2-hydroxynicotinic acid (51 mg, 0.37 mmol) in a 10:1 EtOAc/DMF mixture (6.6 mL), *N*-(3-dimethylaminopropyl)-*N*′-ethylcarbodiimide hydrochloride (EDC·HCl, 99 mg, 0.51 mmol), Et_3N (0.14 mL, 102 mg, 1.00 mmol) and 1-hydroxy-1*H*-benzotriazole (HOBt, 69 mg, 0.51 mmol) were successively added. The mixture was stirred for 10 min at rt, and then treated with a solution of amine **16** (143 mg, 0.34 mmol) in 10:1 EtOAc/DMF (4.4 mL). The reaction mixture was stirred at rt overnight, and then evaporated to dryness. The resulting red oily residue (423 mg) was purified through column chromatography (40−63 μm silica gel, CH_2Cl_2/MeOH/50% aq. NH_4OH mixtures, gradient elution). On elution with CH_2Cl_2/MeOH/50% aq. NH_4OH 98:2:0.4, compound **9** (117 mg, 63% yield) was isolated as a yellowish solid; R_f 0.24 (CH_2Cl_2/MeOH/50% aq. NH_4OH 9.5:0.5:0.04).

A solution of **9** (117 mg) in CH_2Cl_2 (5 mL) was filtered through a 0.2 μm PTFE filter, treated with a methanolic solution of HCl (1.25 M, 2 mL), and evaporated at reduced pressure. The solid was washed with EtOAc (2×5 mL), hexane (2×5 mL), and pentane (2×5 mL), to give, after drying at 45 °C/2 Torr for 72 h, **9**·HCl (88 mg) as a pale brown solid: mp 135−136 °C; IR (ATR) ν 3500−2400 (max at 3247, 3064, 2925, 2854, N−H, $^+$N−H, C−H), 1665, 1630, 1599, 1583, 1554 (C=O, Ar−C−C, Ar−C−N) cm^{-1}; ^{1}H NMR (400 MHz, CD_3OD) δ 1.30−1.48 (complex signal, 10H, 3-H_2, 4-H_2, 5-H_2, 6-H_2, 7-H_2), 1.58 (s, 3H, 9′-CH_3), superimposed 1.58 (m, 2H, 2-H_2), 1.85 (tt, $J = J' = 7.2$ Hz, 2H, 8-H_2), 1.93 (br d, $J = 17.2$ Hz, 1H, 10′-H_{endo}), superimposed in part 1.94 (dm, $J = 12.8$ Hz, 1H, 13′-H_{syn}), 2.08 (dm, $J = 12.8$ Hz, 1H, 13′-H_{anti}), 2.54 (dd, $J = 17.2$ Hz, $J' = 4.4$ Hz, 1H, 10′-H_{exo}), 2.76 (m, 1H, 7′-H), 2.86 (ddd, $J = 18.0$ Hz, $J' = J'' = 2.0$ Hz, 1H, 6′-H_{endo}), 3.20 (dd, $J = 18.0$ Hz, $J' = 5.6$ Hz, 1H, 6′-H_{exo}), 3.37 (t, $J = 7.2$ Hz, 2H, 1-H_2), 3.44 (m, 1H, 11′-H), 3.98 (td, $J = 7.2$ Hz, $J' = 2.8$ Hz, 2H, 9-H_2), 4.85 (s, NH, $^+$NH), 5.58 (br d, $J = 5.2$ Hz, 1H, 8′-H), 6.56 (dd, $J = 7.2$ Hz, $J' = 6.0$ Hz, 1H, pyridone 5-H), 7.54 (dd, $J = 9.2$ Hz, $J' = 2.0$ Hz, 1H, 2′-H), 7.66 (dd, $J = 6.0$ Hz, $J' = 2.0$ Hz, 1H, pyridone 6-H), 7.76 (d, $J = 2.0$ Hz, 1H, 4′-H), 8.39 (d, $J = 9.2$ Hz, 1H, 1′-H), 8.46 (dd, $J = 7.2$ Hz, $J' = 2.0$ Hz, 1H, pyridone 4-H); ^{13}C NMR (100.6 MHz, CD_3OD) δ 23.5 (CH_3, 9′-CH_3), 27.3 (CH, C11′), 27.7 (CH_2), 27.9 (CH_2) (C6, C7), 28.0 (CH, C7′), 29.3 (CH_2, C13′), 30.0 (CH_2), 30.1 (CH_2), 30.37 (CH_2), 30.40 (CH_2) (C2, C3, C4, C5), 31.2 (CH_2, C8), 36.0 (CH_2), 36.1 (CH_2) (C6′, C10′), 40.2 (CH_2, C1), 49.3 (CH_2, C9), 108.3 (CH, pyridone C5), 115.6 (C, C12a′), 117.6 (C, C11a′), 119.1 (CH, C4′), 121.8 (C, pyridone C3), 125.1 (CH, C8′), 126.6 (CH, C2′), 129.5 (CH, C1′), 134.5 (C, C9′), 140.1 (CH, pyridone C6), 140.2 (C, C3′), 141.0 (C, C4a′), 145.8 (CH, pyridone C4), 151.2 (C, C5a′), 157.0 (C, C12′), 164.4 (C, pyridone C2), 166.0 (C, CONH); HRMS (ESI), calcd for [$C_{32}H_{39}^{35}ClN_4O_2$ + H$^+$] 547.2834, found 547.2829; HPLC purity: 99%.

4.2.3. N-{9-[(3-Chloro-6,7,10,11-tetrahydro-9-methyl-7,11-methanocycloocta[b]quinolin-12-yl)amino]nonyl}-1H-pyrazole-4-sulfonamide (10)

A solution of amine **16** (151 mg, 0.35 mmol) and anhydrous Et_3N (0.07 mL, 51 mg, 0.50 mmol) in dry DMF (2.3 mL) was cooled down to 0 °C in an ice/water bath and treated with 1*H*-pyrazole-4-sulfonyl chloride (65 mg, 0.39 mmol). The reaction mixture was stirred at rt overnight. An additional amount of 1*H*-pyrazole-4-sulfonyl chloride (65 mg, 0.39 mmol) was added and the mixture was stirred at rt overnight. The resulting dark yellow solution was evaporated to dryness and the residue was purified through column chromatography (40−63 μm silica gel, CH_2Cl_2/MeOH/50% aq. NH_4OH mixtures, gradient elution). On elution with CH_2Cl_2/MeOH/50% aq. NH_4OH 97:3:0.4, compound **10** (190 mg, 98% yield) was isolated as a yellowish oil; R_f 0.53 (CH_2Cl_2/MeOH/50% aq. NH_4OH 9:1:0.04).

A solution of **10** (190 mg) in CH_2Cl_2 (5 mL) was filtered through a 0.2 μm PTFE filter, treated with a methanolic solution of HCl (1.25 M, 2 mL), and evaporated at reduced pressure. The solid was washed with EtOAc (2×5 mL) and pentane (2×5 mL), to give, after drying at 45 °C/2 Torr for 72 h, **10**·HCl (75 mg) as a pale brown solid: mp 131−133 °C; IR (ATR) ν 3500−2500 (max at 3259, 3119, 2926, 2855, N−H, $^+$N−H, C−H), 1631, 1584, 1570, 1513 (Ar−C−C, Ar−C−N), 1324, 1140 (SO_2) cm^{-1}; ^{1}H NMR (400 MHz, CD_3OD) δ 1.25−1.40 (complex signal, 10H, 3-H_2, 4-H_2, 5-H_2, 6-H_2, 7-H_2), 1.45 (tt, $J = J' = 6.8$ Hz, 2H, 2-H_2), 1.58 (s, 3H, 9′-CH_3), 1.85 (tt, $J = J' = 6.8$ Hz, 2H, 8-H_2), 1.93 (br d, $J = 17.6$ Hz, 1H, 10′-H_{endo}), superimposed in part 1.94 (m, 1H, 13′-H_{syn}), 2.08 (dm, $J = 12.8$ Hz, 1H, 13′-H_{anti}), 2.54 (dm, $J = 17.6$ Hz, 1H, 10′-H_{exo}), 2.77 (m, 1H, 7′-H), 2.85 (dm, $J = 18.0$ Hz, 1H, 6′-H_{endo}), superimposed in part 2.86 (t, $J = 6.8$ Hz, 2H, 1-H_2), 3.20 (dd, $J = 18.0$ Hz, $J' = 5.6$ Hz, 1H, 6′-H_{exo}), 3.43 (m, 1H, 11′-H), 3.98 (t, $J = 6.8$ Hz, 2H, 9-H_2), 4.85 (s, NH, $^+$NH), 5.59 (br d, $J = 5.6$ Hz, 1H, 8′-H), 7.55 (dd, $J = 9.2$ Hz, $J' = 2.0$ Hz, 1H, 2′-H), 7.74 (d, $J = 2.0$ Hz, 1H, 4′-H), 7.97 (br signal, 2H, pyrazole 3-H, pyrazole 5-H), 8.40 (d, $J = 9.2$ Hz, 1H, 1′-H); ^{13}C NMR (100.6 MHz, CD_3OD) δ 23.5 (CH_3, 9′-CH_3), 27.3 (CH, C11′), 27.5 (CH_2), 27.76 (CH_2) (C6, C7), 27.84 (CH, C7′), 29.4 (CH_2, C13′), 29.9 (CH_2), 30.1 (CH_2), 30.3 (CH_2), 30.4 (CH_2) (C2, C3, C4, C5), 31.3 (CH_2, C8), 36.11 (CH_2), 36.15 (CH_2) (C6′, C10′), 44.0 (CH_2, C1), 49.8 (CH_2, C9), 115.7 (C, C12a′), 117.6 (C, C11a′), 119.1 (CH, C4′), 125.2 (CH, C8′), 126.7 (CH, C2′), 129.6 (CH, C1′), 134.5 (C, C9′), 140.2 (C, C3′), 140.9 (C, C4a′), 151.2 (C, C5a′), 156.9 (C, C12′), the signals of the pyrazole carbon atoms were not observed; HRMS (ESI), calcd for [$C_{29}H_{38}^{35}ClN_5O_2S$ + H$^+$] 556.2508, found 556.2511; HPLC purity: 98%.

4.2.4. N-{9-[(3-Chloro-6,7,10,11-tetrahydro-9-methyl-7,11-methanocycloocta[b]quinolin-12-yl)amino]nonyl}-3,5-dihydroxybenzamide (11)

This compound was prepared as described for **9**. From 3,5-dihydroxybenzoic acid (90 mg, 0.58 mmol) and amine **16** (227 mg, 0.53 mmol), a yellow oily residue (759 mg) was obtained and purified through column chromatography (40−63 μm silica gel, CH_2Cl_2/MeOH/50% aq. NH_4OH mixtures, gradient elution). On elution with CH_2Cl_2/MeOH/50% aq. NH_4OH 95:5:0.4, compound **11** (188 mg, 63% yield) was isolated as a yellowish solid; R_f 0.47 (CH_2Cl_2/MeOH/50% aq. NH_4OH 9:1:0.04).

A solution of **11** (188 mg) in CH_2Cl_2 (5 mL) was filtered through a 0.2 μm PTFE filter, treated with a methanolic solution of HCl (1.25 M, 2 mL), and evaporated at reduced pressure. The solid was washed with EtOAc (2×5 mL), hexane (2×5 mL), and pentane (2×5 mL), to give, after drying at 45 °C/2 Torr for 72 h, **11**·HCl (116 mg) as a pale brown solid: mp 159−160 °C; IR (ATR) ν 3500−2400 (max at 3243, 3076, 2926, 2855, O−H, N−H, $^+$N−H, C−H), 1631, 1584, 1512 (C=O, Ar−C−C, Ar−C−N) cm^{-1}; ^{1}H NMR (400 MHz, CD_3OD) δ 1.30−1.48 (complex signal, 10H, 3-H_2, 4-H_2, 5-H_2, 6-H_2, 7-H_2), superimposed in part 1.53−1.63 (m, 2H, 2-H_2), 1.58 (s, 3H, 9′-CH_3), 1.84 (tt, $J = J' = 7.2$ Hz, 2H, 8-H_2), 1.93 (br d, $J = 17.6$ Hz, 1H, 10′-H_{endo}), superimposed in part 1.94 (dm, $J = 12.8$ Hz, 1H, 13′-H_{syn}), 2.08 (dm, $J = 12.8$ Hz, 1H, 13′-H_{anti}), 2.54 (dd, $J = 17.6$ Hz, $J' = 5.6$ Hz, 1H, 10′-H_{exo}), 2.76 (m, 1H, 7′-H), 2.84

(ddd, $J = 17.6$ Hz, $J' = J'' = 2.0$ Hz, 1H, 6'-H$_{endo}$), 3.19 (dd, $J = 17.6$ Hz, $J' = 5.6$ Hz, 1H, 6'-H$_{exo}$), 3.31 (m, 2H, 1-H$_2$), 3.42 (m, 1H, 11'-H), 3.96 (td, $J = 7.2$ Hz, $J' = 3.6$ Hz, 2H, 9-H$_2$), 4.85 (s, NH, $^+$NH, OH), 5.58 (br d, $J = 5.6$ Hz, 1H, 8'-H), 6.38 (dd, $J = J' = 2.0$ Hz, 1H, phenyl 4-H), 6.67 [d, $J = 2.0$ Hz, 2H, phenyl 2(6)-H], 7.55 (dd, $J = 9.2$ Hz, $J' = 2.0$ Hz, 1H, 2'-H), 7.74 (d, $J = 2.0$ Hz, 1H, 4'-H), 8.38 (d, $J = 9.2$ Hz, 1H, 1'-H); ^{13}C NMR (100.6 MHz, CD$_3$OD) δ 23.5 (CH$_3$, 9'-CH$_3$), 27.3 (CH, C11'), 27.7 (CH$_2$), 27.8 (CH$_2$) (C6, C7), 27.9 (CH, C7'), 29.3 (CH$_2$, C13'), 30.0 (CH$_2$), 30.1 (CH$_2$), 30.4 (2CH$_2$) (C2, C3, C4, C5), 31.2 (CH$_2$, C8), 36.0 (CH$_2$), 36.1 (CH$_2$) (C6', C10'), 40.8 (CH$_2$, C1), 49.5 (CH$_2$, C9), 106.4 (CH, phenyl C4), 106.7 [2CH, phenyl C2(6)], 115.6 (C, C12a'), 117.6 (C, C11a'), 119.1 (CH, C4'), 125.1 (CH, C8'), 126.6 (CH, C2'), 129.4 (CH, C1'), 134.5 (C, C9'), 138.0 (C, phenyl C1), 140.2 (C, C3'), 140.9 (C, C4a'), 151.1 (C, C5a'), 156.9 (C, C12'), 159.8 [2C, phenyl C3(5)], 170.5 (C, CONH); HRMS (ESI), calcd for [C$_{33}$H$_{40}^{35}$ClN$_3$O$_3$ + H$^+$] 562.2831, found 562.2825; HPLC purity: 98%.

4.2.5. 9-[(3-Chloro-6,7,10,11-tetrahydro-9-methyl-7,11-methanocycloocta[b]quinolin-12-yl)amino]-N-(1H-pyrazol-4-yl)nonanamide (12)

A solution of nitrile **15** (619 mg, 1.47 mmol) in MeOH (7.5 mL) was treated with a 40% methanolic solution of KOH (9 mL). The resulting suspension was stirred under reflux for 48 h, then treated with water (5 mL), and stirred under reflux overnight. The resulting solution was cooled to rt and evaporated in vacuo. The resulting residue was treated with 5 N HCl (25 mL), and the mixture was concentrated at reduced pressure, to give the corresponding carboxylic acid in the form of hydrochloride salt (4.06 g), which was used in the following step without further purification.

To a suspension of crude carboxylic acid (2.03 g of a crude that could contain a maximum of 350 mg, 0.73 mmol of acid) in a 10:1 EtOAc/DMF mixture (13.2 mL), EDC·HCl (210 mg, 1.10 mmol), Et$_3$N (0.4 mL, 290 mg, 2.87 mmol), and HOBt (149 mg, 1.10 mmol) were successively added. The resulting mixture was stirred at rt for 15 min, and then treated with a suspension of 4-amino-1H-pyrazole (67 mg, 0.81 mmol) in 10:1 EtOAc (11 mL). The reaction mixture was stirred at rt overnight. The resulting mixture was diluted with EtOAc (18 mL) and washed with water (3 × 45 mL) and brine (45 mL). The organic phase was dried over anhydrous Na$_2$SO$_4$ and evaporated to dryness to afford a brown oil (212 mg), which was purified through column chromatography (40–63 μm silica gel, CH$_2$Cl$_2$/MeOH/50% aq. NH$_4$OH mixtures, gradient elution). On elution with CH$_2$Cl$_2$/MeOH/50% aq. NH$_4$OH 97:3:0.4, compound **12** (175 mg, 47% yield) was isolated as a yellow oil; R_f 0.14 (CH$_2$Cl$_2$/MeOH/50% aq. NH$_4$OH 9.5:0.5:0.04).

A solution of **12** (175 mg) in CH$_2$Cl$_2$ (2 mL) was filtered through a 0.2 μm PTFE filter, treated with a methanolic solution of HCl (1.25 M, 2 mL), and evaporated at reduced pressure. The solid was washed with EtOAc (2 × 5 mL) and pentane (2 × 5 mL) to give, after drying at 45 °C/2 Torr for 7 days, **12**·HCl (149 mg) as a pale brown solid: mp 141–142 °C; IR (ATR) ν 3500–2400 (max at 3237, 3058, 2926, 2854, N–H, $^+$N–H, C–H), 1733, 1671, 1630, 1583, 1568, 1512 (C=O, Ar–C–C, Ar–C–N) cm^{-1}; ^{1}H NMR (400 MHz, CD$_3$OD) δ 1.28–1.48 (complex signal, 8H, 4-H$_2$, 5-H$_2$, 6-H$_2$, 7-H$_2$), 1.58 (s, 3H, 9'-CH$_3$), 1.68 (m, 2H, 3-H$_2$), 1.86 (m, 2H, 8-H$_2$), 1.93 (br d, $J = 18.0$ Hz, 1H, 10'-H$_{endo}$), superimposed in part 1.94 (dm, $J = 12.4$ Hz, 1H, 13'-H$_{syn}$), 2.08 (dm, $J = 12.4$ Hz, 1H, 13'-H$_{anti}$), 2.36 (t, $J = 7.2$ Hz, 2H, 2-H$_2$), 2.55 (dm, $J = 18.0$ Hz, 1H, 10'-H$_{exo}$), 2.77 (m, 1H, 7'-H), 2.85 (br d, $J = 17.6$ Hz, 1H, 6'-H$_{endo}$), 3.20 (dd, $J = 17.6$ Hz, $J' = 5.2$ Hz, 1H, 6'-H$_{exo}$), 3.44 (m, 1H, 11'-H), 3.98 (t, $J = 7.2$ Hz, 2H, 9-H$_2$), 4.85 (s, NH, $^+$NH), 5.59 (br d, $J = 5.2$ Hz, 1H, 8'-H), 7.56 (dd, $J = 9.2$ Hz, $J' = 1.6$ Hz, 1H, 2'-H), 7.75 (d, $J = 1.6$ Hz, 1H, 4'-H), 8.12 (br signal, 2H, pyrazole 3-H, pyrazole 5-H), 8.40 (d, $J = 9.2$ Hz, 1H, 1'-H); ^{13}C NMR (100.6 MHz, CD$_3$OD) δ 23.5 (CH$_3$, 9'-CH$_3$), 25.9 (CH$_2$, C3), 26.6 (CH, C11'), 27.3 (CH$_2$, C4), 27.8 (CH, C7'), 29.4 (CH$_2$, C13'), 30.11 (CH$_2$),

30.14 (CH$_2$), 30.3 (CH$_2$) (C5, C6, C7), 31.3 (CH$_2$, C8), 36.1 (CH$_2$), 36.2 (CH$_2$) (C6', C10'), 37.1 (CH$_2$, C2), 49.8 (CH$_2$, C9), 115.7 (C, C12a'), 117.6 (C, C11a'), 119.2 (CH, C4'), 125.2 (CH, C8'), 126.7 (CH, C2'), 129.6 (CH, C1'), 134.5 (C, C9'), 140.1 (C, C3'), 140.9 (C, C4a'), 151.2 (C, C5a'), 156.9 (C, C12'), 173.8 (C, C1), the signals of the pyrazole carbon atoms were not observed; HRMS (ESI), calcd for [C$_{29}$H$_{36}^{35}$ClN$_5$O + H$^+$] 506.2681, found 506.2681; HPLC purity: 96%.

4.2.6. 4-{9-[(3-Chloro-6,7,10,11-tetrahydro-9-methyl-7,11-methanocycloocta[b]quinolin-12-yl)amino]nonanoyl}piperazin-2-one (13)

This compound was prepared as described for **12**. From nitrile **15** (232 mg, 0.55 mmol), crude carboxylic acid (1.99 g) was obtained as the hydrochloride salt and used in the following step without further purification. From this crude carboxylic acid and piperazin-2-one (60 mg, 0.60 mmol), a brown oily residue (2.64 g) was obtained and subjected to column chromatography purification (40–63 μm silica gel, CH$_2$Cl$_2$/MeOH/50% aq. NH$_4$OH mixtures, gradient elution). On elution with CH$_2$Cl$_2$/MeOH/50% aq. NH$_4$OH 98:2:0.4, compound **13** (187 mg, 65% yield) was isolated as a yellow oil; R_f 0.25 (CH$_2$Cl$_2$/MeOH/50% aq. NH$_4$OH 9.6:0.4:0.04).

A solution of **13** (187 mg) in CH$_2$Cl$_2$ (2 mL) was filtered through a 0.2 μm PTFE filter, treated with a methanolic solution of HCl (1.25 M, 2 mL), and evaporated at reduced pressure. The solid was washed with EtOAc (2 × 5 mL) and pentane (2 × 5 mL) to give, after drying at 45 °C/2 Torr for 7 days, **13**·HCl (147 mg) as a pale brown solid: mp 92–95 °C; IR (ATR) ν 3500–2400 (max at 3245, 3054, 3010, 2926, 2854, N–H, $^+$N–H, C–H), 1743, 1630, 1583, 1513 (C=O, Ar–C–C, Ar–C–N) cm^{-1}; ^{1}H NMR (400 MHz, CD$_3$OD) δ 1.30–1.48 (complex signal, 8H, 4-H$_2$, 5-H$_2$, 6-H$_2$, 7-H$_2$), 1.59 (s, 3H, 9'-CH$_3$), superimposed 1.55–1.64 (m, 2H, 3-H$_2$), 1.86 (tt, $J = J' = 6.8$ Hz, 2H, 8-H$_2$), 1.93 (br d, $J = 18.0$ Hz, 1H, 10'-H$_{endo}$), superimposed in part 1.94 (dm, $J = 12.8$ Hz, 1H, 13'-H$_{syn}$), 2.09 (dm, $J = 12.8$ Hz, 1H, 13'-H$_{anti}$), 2.29 (t, $J = 7.2$ Hz, 2H, 2-H$_2$), 2.55 (dd, $J = 18.0$ Hz, $J' = 5.2$ Hz, 1H, 10'-H$_{exo}$), 2.77 (m, 1H, 7'-H), 2.87 (dm, $J = 18.0$ Hz, 1H, 6'-H$_{endo}$), 3.14 (m, 2H, piperazinone 6-H$_2$), 3.21 (dd, $J = 18.0$ Hz, $J' = 5.6$ Hz, 1H, 6'-H$_{exo}$), 3.45 (m, 1H, 11'-H), 3.67 (m, 2H, piperazinone 5-H$_2$), 3.79 (s, 2H, piperazinone 3-H$_2$), 3.98 (br t, $J = 7.2$ Hz, 2H, 9-H$_2$), 4.85 (s, NH, $^+$NH), 5.59 (br d, $J = 5.6$ Hz, 1H, 8'-H), 7.56 (dd, $J = 9.2$ Hz, $J' = 2.0$ Hz, 1H, 2'-H), 7.79 (d, $J = 2.0$ Hz, 1H, 4'-H), 8.40 (d, $J = 9.2$ Hz, 1H, 1'-H); ^{13}C NMR (100.6 MHz, CD$_3$OD) δ 23.5 (CH$_3$, 9'-CH$_3$), 25.8 (CH$_2$, C3), 27.3 (CH, C11'), 27.7 (CH$_2$, C4), 27.9 (CH, C7'), 29.3 (CH$_2$, C13'), 30.1 (2CH$_2$), 30.4 (CH$_2$) (C5, C6, C7), 31.3 (CH$_2$, C8), 33.8 (CH$_2$, C2), 36.0 (CH$_2$), 36.1 (CH$_2$) (C6', C10'), 38.8 (CH$_2$, piperazinone C6), 46.8 (CH$_2$, piperazinone C5), 49.7 (CH$_2$, C9), 53.2 (CH$_2$, piperazinone C3), 115.7 (C, C12a'), 117.6 (C, C11a'), 119.1 (CH, C4'), 125.1 (CH, C8'), 126.6 (CH, C2'), 129.5 (CH, C1'), 134.5 (C, C9'), 140.2 (C, C3'), 141.0 (C, C4a'), 151.2 (C, C5a'), 156.9 (C, C12'), 172.2 (C), 177.6 (C) (C1, piperazinone C2); HRMS (ESI), calcd for [C$_{30}$H$_{39}^{35}$ClN$_4$O$_2$ + H$^+$] 523.2834, found 523.2839; HPLC purity: 96%.

4.2.7. 9-[(3-Chloro-6,7,10,11-tetrahydro-9-methyl-7,11-methanocycloocta[b]quinolin-12-yl)amino]-N-[(2-methoxy-4-pyridyl)methyl]nonanamide (17)

This compound was prepared as described for **12**. From nitrile **15** (619 mg, 1.47 mmol), crude carboxylic acid (4.06 g) was obtained as the hydrochloride salt and used in the following step without further purification. From crude carboxylic acid (2.03 g of a crude that could contain a maximum of 350 mg, 0.73 mmol of acid) and (2-methoxy-4-pyridyl)methanamine (112 mg, 0.81 mmol), a brown oily residue (396 mg) was obtained and subjected to column chromatography purification (40–63 μm silica gel, CH$_2$Cl$_2$/MeOH/50% aq. NH$_4$OH mixtures, gradient elution). On elution with CH$_2$Cl$_2$/MeOH/50% aq. NH$_4$OH 98:2:0.7, compound **17** (246 mg, 60% yield) was isolated as a yellow oil.

A solution of **17** (141 mg) in MeOH (15 mL) was washed with hexane (2 × 10 mL) and pentane (10 mL), and then evaporated at reduced pressure. After drying at 45 °C/2 Torr for 72 h, the analytical sample of **17** (103 mg) was obtained as a brown oil: R_f 0.45 CH$_2$Cl$_2$/MeOH/50% aq. NH$_4$OH 9.5:0.5:0.04); IR (ATR) ν 3283, 3061 (N–H), 1655, 1611, 1557 (C=O, Ar–C–C, Ar–C–N) cm^{-1}; ^{1}H NMR (400 MHz, CD$_3$OD) δ 1.28–1.40 (complex signal, 8H, 4-H$_2$, 5-H$_2$, 6-H$_2$, 7-H$_2$), 1.52 (s, 3H, 9′-CH$_3$), 1.61 (tt, $J = J' = 7.2$ Hz, 2H, 3-H$_2$), 1.71 (tt, $J = J' = 7.2$ Hz, 2H, 8-H$_2$), 1.85 (br d, $J = 17.6$ Hz, 1H, 10′-H$_{endo}$), superimposed in part 1.91 (dm, $J = 12.4$ Hz, 1H, 13′-H$_{syn}$), 2.05 (dm, $J = 12.4$ Hz, 1H, 13′-H$_{anti}$), 2.24 (t, $J = 7.2$ Hz, 2H, 2-H$_2$), 2.53 (dd, $J = 17.6$ Hz, $J' = 5.6$ Hz, 1H, 10′-H$_{exo}$), 2.69 (m, 1H, 7′-H), 2.89 (dd, $J = 17.6$ Hz, $J' = J'' = 2.0$ Hz, 1H, 6′-H$_{endo}$), 3.08 (dd, $J = 17.6$ Hz, $J' = 5.6$ Hz, 1H, 6′-H$_{exo}$), 3.43 (m, 1H, 11′-H), 3.57 (br t, $J = 7.2$ Hz, 2H, 9-H$_2$), 3.86 (s, 3H, OCH$_3$), 4.32 (s, 2H, pyridine-CH$_2$-NHCO), 4.85 (s, NH), 5.54 (br d, $J = 5.2$ Hz, 1H, 8′-H), 6.66 (dd, $J = 1.6$ Hz, $J' = 0.8$ Hz, 1H, pyridine 3-H), 6.84 (dd, $J = 5.2$ Hz, $J' = 1.6$ Hz, 1H, pyridine 5-H), 7.31 (dd, $J = 9.2$ Hz, $J' = 2.0$ Hz, 1H, 2′-H), 7.72 (d, $J = 2.0$ Hz, 1H, 4′-H), 8.02 (dd, $J = 5.2$ Hz, $J' = 0.8$ Hz, 1H, pyridine 6-H), 8.08 (d, $J = 9.2$ Hz, 1H, 1′-H); ^{13}C NMR (100.6 MHz, CD$_3$OD) δ 23.6 (CH$_3$, 9′-CH$_3$), 26.9 (CH$_2$, C3), 27.9 (CH$_2$, C4), 28.4 (CH, C11′), 29.5 (CH, C7′), 30.1 (2CH$_2$), 30.20 (CH$_2$), 30.25 (CH$_2$) (C5, C6, C7, C13′), 32.2 (CH$_2$, C8), 36.9 (CH$_2$, C2), 37.8 (CH$_2$, C10′), 40.4 (CH$_2$, C6′), 42.8 (CH$_2$, pyridine-CH$_2$-NHCO), 50.8 (CH$_2$, C9), 54.1 (CH$_3$, OCH$_3$), 109.6 (CH, pyridine C3), 116.9 (CH, pyridine C5), 119.7 (C, C12a′), 121.6 (C, C11a′), 124.9 (CH, C2′), 126.1 (CH, C8′), 126.4 (CH, C4′), 127.5 (CH, C1′), 133.7 (2C), 135.7 (C) (pyridine C4, C4a′, C9′), 147.7 (CH, pyridine C6), 148.8 (C, C3′), 153.0 (C), 153.1 (C) (C5a′, C12′), 159.0 (C, pyridine C2), 176.4 (C, C1); HRMS (ESI), calcd for [C$_{33}$H$_{41}^{35}$ClN$_4$O$_2$ + H$^+$] 561.2991, found 561.2985; HPLC purity: 95%.

4.2.8. 9-[(3-Chloro-6,7,10,11-tetrahydro-9-methyl-7,11-methanocycloocta[b]quinolin-12-yl)amino]-N-[(2-oxo-1,2-dihydro-4-pyridyl)methyl]nonanamide (14)

To a solution of compound **17** (95 mg, 0.17 mmol) in DMF (1 mL), LiCl (32 mg, 0.75 mmol) and *p*-toluenesulfonic acid monohydrate (144 mg, 0.75 mmol) were added. The reaction mixture was stirred at 120 °C for 35 min, cooled down to rt, diluted with H$_2$O (2 mL) and sat. aq. NaHCO$_3$ (5 mL) and extracted with EtOAc (3 × 5 mL). The combined organic extracts were washed with H$_2$O (3 × 7 mL), dried over anhydrous Na$_2$SO$_4$, and evaporated to dryness to afford **14** (44 mg, 48% yield) as a brown oil; R_f 0.41 (CH$_2$Cl$_2$/MeOH/50% aq. NH$_4$OH 9:1:0.04).

A solution of **14** (44 mg) in CH$_2$Cl$_2$ (2 mL) was filtered through a 0.2 μm PTFE filter, treated with a methanolic solution of HCl (1.25 M, 2 mL), and evaporated at reduced pressure. The solid was washed with EtOAc (2 × 5 mL), hexane (2 × 5 mL), and pentane (2 × 5 mL) to give, after drying at 45 °C/2 Torr for 72 h, **14**·HCl (45 mg) as an off-white solid: mp 132–134 °C; IR (ATR) ν 3500–2400 (max at 3245, 3058, 2926, 2854, N–H, $^+$N–H, C–H), 1650, 1632, 1583, 1568, 1516 (C=O, Ar–C–C, Ar–C–N) cm^{-1}; ^{1}H NMR (400 MHz, CD$_3$OD) δ 1.30–1.48 (complex signal, 8H, 4-H$_2$, 5-H$_2$, 6-H$_2$, 7-H$_2$), 1.58 (s, 3H, 9′-CH$_3$), 1.64 (m, 2H, 3-H$_2$), 1.86 (tt, $J = J' = 7.6$ Hz, 2H, 8-H$_2$), 1.93 (br d, $J = 18.0$ Hz, 1H, 10′-H$_{endo}$), superimposed in part 1.94 (dm, $J = 12.4$ Hz, 1H, 13′-H$_{syn}$), 2.08 (dm, $J = 12.4$ Hz, 1H, 13′-H$_{anti}$), 2.28 (t, $J = 7.2$ Hz, 2H, 2-H$_2$), 2.54 (dm, $J = 18.0$ Hz, 1H, 10′-H$_{exo}$), 2.77 (m, 1H, 7′-H), 2.86 (br d, $J = 18.0$ Hz, 1H, 6′-H$_{endo}$), 3.20 (dd, $J = 18.0$ Hz, $J' = 5.6$ Hz, 1H, 6′-H$_{exo}$), 3.45 (m, 1H, 11′-H), 3.98 (t, $J = 7.6$ Hz, 2H, 9-H$_2$), 4.31 (s, 2H, pyridone-CH$_2$-NHCO), 4.85 (s, NH, $^+$NH), 5.58 (br d, $J = 5.6$ Hz, 1H, 8′-H), 6.55 (br signal, 2H, pyridone 3-H, pyridone 5-H), 7.55 (dd, $J = 9.2$ Hz, $J' = 2.0$ Hz, 1H, 2′-H), superimposed in part 7.59 (br s, 1H, pyridone 6-H), 7.76 (d, $J = 2.0$ Hz, 1H, 4′-H), 8.40 (d, $J = 9.2$ Hz, 1H, 1′-H); ^{13}C NMR (100.6 MHz, CD$_3$OD) δ 23.5 (CH$_3$, 9′-CH$_3$), 26.8 (CH$_2$, C3), 27.3 (CH, C11′), 27.7 (CH$_2$, C4), 27.8 (CH, C7′), 29.3 (CH$_2$, C13′), 30.1 (CH$_2$),

30.16 (CH$_2$), 30.24 (CH$_2$) (C5, C6, C7), 31.2 (CH$_2$, C8), 36.0 (CH$_2$, C6′), 36.1 (CH$_2$, C10′), 36.9 (CH$_2$, C2), 43.1 (CH$_2$, pyridone-CH$_2$-NHCO), 49.7 (CH$_2$, C9), 110.4 (2CH, pyridone C3, pyridone C5), 115.6 (C, C12a′), 117.6 (C, C11a′), 119.1 (CH, C4′), 125.1 (CH, C8′), 126.7 (CH, C2′), 129.5 (CH, C1′), 134.5 (C, C9′), 136.3 (CH, pyridone C6), 140.2 (C, C3′), 141.0 (C, C4a′), 151.2 (C, C5a′), 156.9 (C, C12′), 158.5 (C, pyridone C2), 176.5 (C, C1), the signal of pyridone C4 was not observed; HRMS (ESI), calcd for [C$_{32}$H$_{39}^{35}$ClN$_4$O$_2$ + H$^+$] 547.2834, found 547.2830; HPLC purity: 96%.

4.3. In vitro determination of hBACE-1 inhibitory activity

The inhibition of human recombinant BACE-1 (β-secretase, Invitrogen) by the new hybrids was evaluated following a standard methodology [10,82], using 10 μL of substrate (Panvera peptide at a 250 nM final concentration), 10 μL of solution of the inhibitors or buffer in control wells with 20 mM sodium acetate, pH 4.5, and 0.1% w/v CHAPS, and adding 10 μL of hBACE-1 (12.91 mU) to initiate the enzymatic reaction, which was left for 1 h at 37 °C. Ten μL of STOP solution (2.5 M sodium acetate) were added and the fluorescence signal was read at $\lambda_{em} = 544$ nm ($\lambda_{ex} = 590$ nm). The hBACE-1 inhibitory activity of the compounds was calculated as follows: $100 - (IF_i/IF_0 \times 100)$, in which IF_i and IF_0 are the fluorescence intensities in the presence and in the absence of inhibitor, respectively. For a more detailed description of the assay see the Supplementary Data.

4.4. Molecular dynamics simulations of the binding mode within hBACE-1

The binding modes of compounds **10** and **11** into the active site of BACE-1 were investigated by means of MD simulations. The effect of chirality at the level of huprine moiety was also examined. Accordingly, four ligands, namely (7R,11R)-**10**, (7S,11S)-**10**, (7R,11R)-**11**, and (7S,11S)-**11** were simulated.

The previously reported poses for both enantiomers of the rhein–huprine hybrid **1** were used as reference to manually dock the four new hybrids into the BACE-1 catalytic site [21]. Parameters for the four ligands in their bioactive conformation were then calculated using the GAFF force field [83] and RESP [84] charges were determined at the B3LYP/6-31G(d) level with Gaussian 09 [85].

Reference starting geometries for BACE-1 and the general setting for MD simulations were taken from our previous works [21]. Briefly, acetyl (ACE) and *N*-methyl (NME) capping groups were added to neutralize the N- and C-termini of the protein. The catalytic dyad was simulated with neutral (ASH) Asp 228 and charged (ASP) Asp 32, and three disulfide bridges were defined between cysteine residues 155–359, 217–382, and 269–319. The amber ff99SB-ILDN force field was used to describe the protein [86,87]. About 20,800 TIP3P [88] water molecules and 9 Na$^+$ counterions were added to solvate and neutralize each system, which was simulated in a truncated octahedron box with a layer of 18 Å for a total of about 69,000 atoms.

Prior to MD simulations, systems were energy minimized by applying 50,000 steps of the steepest descent algorithm followed by 5000 steps of conjugate gradient algorithm. One ns of MD simulation in the NVT ensemble was performed by using the velocity-rescaling thermostat [89] with a 0.1 ps time constant for thermal coupling to heat the system from 0 to 300 K. A positional restraint with a force constant of 1000 kJ mol^{-1} nm^{-2} was applied to the protein backbone atoms to avoid artefactual distortions during the heating. Finally, 5 ns of MD simulation in the NPT ensemble by using the Parrinello-Rahman barostat [90] with a 0.5 ps time constant for coupling were run to properly equilibrate the

density of the system. Finally, 300 ns of MD production at constant volume (v-rescale) and temperature (330 K) using periodic boundary conditions were run for each system with Gromacs2018 [32]. The LINCS method [91], which is up to four times more rapid than the SHAKE algorithm, was applied to constraint bonds involving hydrogen atoms. A cutoff of 1.2 nm was used to treat short-range non-bonded interactions, and the Particle Mesh Ewald (PME) method was applied to long-range electrostatic interactions [92]. A time step of 2 fs was used along the simulation. The *rms* and *distance* modules of Gromacs2018 were finally used to analyze trajectories.

Molecular properties (clogP, percentage of polar surface) of the 3,5-dihydroxybenzamide, pyrazole-sulfonamide and amidated rhein-carboxamide moieties of compounds **11**, **10**, and **1**, respectively, were determined using Datawarrior [93] and ChemAxon [94].

4.5. In vitro determination of hAChE and hBChE inhibitory activity

The *in vitro* anticholinesterase activity of the new hybrids was determined by a well-established spectrophotometric method [38], using human recombinant AChE (dissolved in 0.1% Triton X-100/0.1 M potassium phosphate, pH 8.0) or human serum BChE (dissolved in 0.1% aq. gelatin), and 1 mM stock solutions of the inhibitors in MeOH, as previously reported [10]. For the enzymatic reaction, a mixture of 5,5′-dithiobis(2-nitrobenzoic acid) (340 μM) and the enzyme (0.02 unit/mL) in 0.1 M potassium phosphate at pH 8.0 were preincubated with different concentrations of the inhibitors at 37 °C for 20 min, and thereafter the substrate acetylthiocholine iodide or butyrylthiocholine iodide (550 μM) was added. For a more detailed description of the assay see the Supplementary Data.

4.6. Determination of the Aβ42 and tau antiaggregating activity in intact E. coli cells

The inhibitory activities of the target compounds towards Aβ42 and tau aggregation were assessed using intact *E. coli* cells, following a previously reported methodology [39,43,93]. For the Aβ42 aggregation assay, *E. coli* BL21 (DE3) competent cells were transformed with the pET28a vector (Novagen, Inc., Madison, WI, USA), carrying the DNA sequence of Aβ42. For the tau aggregation assay, *E. coli* BL21 (DE3) competent cells were transformed with pTARA, containing the RNA-polymerase gen of T7 phage (T7RP) under the control of the promoter PBAD, and were then transformed with the pRKT42 vector, encoding four repeats of tau protein in two inserts. The Aβ42 and tau anti-aggregating activity of the target compounds (at a final concentration of 10 μM) was assessed by a fluorescence assay [39,43,95], using Th–S (T1892, Sigma, St. Louis, MO, USA) to monitor Aβ42 and tau aggregation. For a more detailed description of the assay see the Supplementary Data.

4.7. Biometals chelation assays

UV–Vis spectra were measured in 20 mM HEPES buffer (pH = 7.4, 150 mM NaCl) using crystal clear polysterene cuvettes (1.5 mL, 12.5 × 12.5 × 24 mm W × D × H) and a spectrophotometer (Shimadzu UVmini-1240). Aqueous $CuSO_4$, $ZnCl_2$, $FeCl_2$ solutions were freshly prepared before use. For the complexation assays, 20 μL of compound (3 mM) in DMSO were combined with 960 μL of HEPES buffer. Then, 20 μL of aqueous metal solution (3 mM) were added, mixed and incubated at rt for 20 min. Compounds and metals were in equimolar concentrations (60 μM). The addition of 20 μL DMSO instead of compound solution served as blank. Metal chelation was detected as change in the UV–Vis absorption spectra.

4.8. Cu²⁺ chelation ability

The ability of the target compounds to chelate Cu^{2+} was assessed using pyrocatechol violet (PV, Sigma-Aldrich, Darmstadt, Germany), which forms a colored complex in the presence of Cu^{2+}. Compound stock solutions were prepared in DMSO (3 mM), PV solution (600 μM) in sodium acetate buffer (50 mmol/L, pH 6.0), and Cu^{2+} solution (300 μM) was prepared from $CuSO_4$ dissolved in a mixture of sodium acetate buffer and 70% DMSO. As a reference compound, commercially available 0.1 M aqueous EDTA-disodium salt standard solution (Merck, Darmstadt, Germany) was used. The experiment was performed in a 96-well plate. In order to obtain different compound/Cu^{2+} ratios (5:1, 2:1, 1:1, 0.5:1), compound stock solutions were diluted with sodium acetate buffer, and to 50 μL of dilution 50 μL Cu^{2+} solution (300 μM) was added. Blank absorbance at 632 nm was determined using a multiwell plate photometer (Tecan, SpectraMax 250). Then, 50 μL of PV solution (600 μM) were added, using a 12-channel pipette and the absorbance was directly measured. For control, 50 μL DMSO instead of compound solution were used. The Cu^{2+} chelating ability was calculated using the following equation:

$$Cu^{2+}\,chelation\,ability(\%) = 100$$
$$-\frac{A_{sample} - (A_{blank\,sample} + A_{PV})}{A_{control} - A_{PV}} * 100$$

With A_{PV}: 50 μL DMSO, 50 μL sodium acetate buffer (containing 70% DMSO) and 50 μL of PV.

Data are expressed as mean ± SD of three independent experiments, each performed in duplicate. Analysis was accomplished using GraphPad Prism 5 software.

4.9. DPPH assay

2,2-Diphenyl-1-picrylhydrazyl (DPPH), ascorbic acid, and HPLC pure MeOH and DMSO were purchased from Sigma-Aldrich (Darmstadt, Germany). Stock solutions of standard antioxidant ascorbic acid and target compounds were prepared in DMSO (3 mM). DPPH solution was daily fresh prepared in MeOH and stored in the dark. A dilution row of compound in MeOH ranging over 9 dilutions 1−500 μM was prepared in a 96-well plate using a multichannel-pipette. Blank was measured at 517 nm using a multiwell plate photometer (Tecan, SpectraMax 250). To 100 μL compound dilution, 33.3 μL methanolic DPPH solution (200 μM) were added, using a multichannel pipette. The 96-well plate was incubated at rt in the dark for 30 min. After incubation, absorbance was measured at 517 nm. MeOH (100 μL) and DPPH (33.3 μL, 200 μM) served as negative control. The percentage of DPPH radical scavenging activity (SCV) was calculated by the following equation:

$$SCV(\%) = \frac{A_{neg.control} - (A_{sample} - A_{blank})}{A_{neg.control}} * 100$$

For active compounds, concentration-dependent SCV curves were calculated using a non-linear fit and EC_{50} values were then determined graphically using GraphPad Prism 5 software. For compounds that showed no plateau at high concentration, but a concentration-dependent absorption decrease, the SCV at the highest tested concentration was calculated. Data are expressed as mean ± SD of at least two independent experiments, each performed in duplicate.

4.10. Neuroprotection and neurotoxicity assay in HT22 cells

The neuroprotective activity and the neurotoxicity of the novel compounds was assessed by incubating HT22 mouse hippocampal neuronal cells in the presence of different concentrations of the compounds (+5 mM glutamate in the case of the neuroprotection assay), following a previously reported methodology [35]. Cell viability was measured in all cases by the 3-(4,5-dimethylthiazol-2-yl)-2,5-diphenyl tetrazolium bromide (MTT, Sigma-Aldrich, Darmstadt, Germany) assay. For a more detailed description of the assay see the Supplementary Data.

4.11. Zebrafish embryo acute toxicity assay

Maintenance of adult zebrafish was approved by the Ethical Committee for Animal Experimentation of the University of Barcelona (CEEA), accepted by the Department of Environment and Housing of the Generalitat de Catalunya with the license number 334/18, and according to the Generalitat de Catalunya Decree 214/1997 of 30 July, which regulates the use of animals for experimental and other scientific purposes.

The zebrafish embryo acute toxicity assay was conducted following the OECD Guideline number 236: Fish Embryo Acute Toxicity (FET) Test [54] with modifications as described in Barenys et al. [58]. Briefly, eggs were harvested between 1 and 2 h after spawning, were collected, cleaned with OECD water diluted 1:5 as specified in ISO 7346−1 and 7346−2 (ISO, 1996; 2 mM $CaCl_2 \cdot 2H_2O$; 0.5 mM $MgSO_4 \cdot 7H_2O$; 0.75 mM $NaHCO_3$; 0.07 mM KCl) and selected under a dissection stereomicroscope. Fertilized and synchronously divided zebrafish embryos were randomly distributed in 6-well plates (10 embryos/well), cleaned once more with OECD water diluted 1:5, and exposed to the different concentrations of the testing compounds diluted in Danieau's solution 0.3X (5 mL/well; 17.4 mM NaCl; 0.23 mM KCl; 0.12 mM $MgSO_4 \cdot 7H_2O$; 0.18 mM $Ca(NO_3)_2$; 1.5 mM HEPES; pH 7.4) with a constant final DMSO concentration of 1%. Testing solutions were always prepared directly before the start of each experiment and were renewed every 24 h. In all cases, the maximum concentration tested was 100 μM and 4 concentrations more were prepared by a dilution factor 1:2. In those cases where this concentration range was producing more than 75% of lethality in four out of the five concentrations tested, a dilution factor 1:10 was applied and the maximum tested concentration was established at 10 μM. Control condition always included 1% DMSO as vehicle control.

Six-well plates were incubated in a room with controlled temperature (26 ± 1 °C) and light cycle (14 h light: 10 h darkness) for 72 h. Every 24 h lethality was evaluated following the four parameters described in the OECD Guideline n. 236: coagulation of the embryo, lack of somite formation, non-detachment of the tail, or lack of heartbeat (only from 48 h on). Percentage of lethality in each concentration was recorded and the mean ± SEM of the results of at least three independent experiments was calculated in order to determine the lowest observed adverse effective concentration (LOAEC), defined as the lowest concentration with significant adverse effects for lethality, and the lethal concentration killing 50% individuals (LC_{50}) using GraphPad Prism® software v8. LOAEC was calculated with ANOVA test and Bonferroni's post-hoc test for multiple comparison with a significance threshold established at $p < 0.05$. LC_{50} was calculated by adjusting the results of the means of the six tested groups of at least three experiments per compound to a non-linear concentration-response curve with variable slope and least squares fit with minimum and maximum fixed values at 0 and 100% of lethality.

4.12. In vitro brain permeability: PAMPA-BBB assay

The in vitro parallel artificial membrane permeability assay for blood–brain barrier penetration (PAMPA-BBB) described Di et al. [59] was employed to determine the permeability (P_e) of the novel hybrids (dissolved in PBS/EtOH 70:30) across a lipid extract of porcine brain membrane. After assay validation with known drugs (Supplementary Table S6), the cutoff values for high, low and uncertain brain permeation were set at P_e (10^{-6} cm/s) > 5.21, P_e (10^{-6} cm/s) < 1.93, and 5.21 > P_e (10^{-6} cm/s) > 1.93, respectively. For a more detailed description of the assay see the Supplementary Data.

4.13. Aqueous solubility screen

This assay was performed at the Innopharma Drug Screening and Pharmacogenomics Platform (Santiago de Compostela, Spain). Stock solutions of the tested compounds (10^{-2} M) were diluted to decreased molarity, from 300 μM to 0.1 μM, in a 384 well transparent plate (Greiner 781,801) with 1% DMSO: 99% PBS, incubated at 37 °C and read after 2 h in a NEPHELOstar Plus (BMG LABTECH).

The results were adjusted to a segmented regression to obtain the maximum concentration in which the compounds were soluble.

4.14. Chronic in vivo efficacy studies

4.14.1. Animals and treatment

Seven month-old SAMR1 (n = 10) and SAMP8 (n = 20) male mice were used to perform behavioral tests and molecular analyses. Animals were randomly divided into SAMR1 control (SR1 Ct; n = 10), SAMP8 control (SP8 Ct; n = 10) and SAMP8 treated (SP8 11; n = 10) with compound **11** (2 mg/kg/day). The animals had free access to food and water and were kept under standard temperature conditions (22 ± 2 °C) and 12-h/12-h light/dark cycles (300 lux/0 lux). Compounds were dissolved in 1.8% (2-hydroxypropyl)-β-cyclodextrin and administered through drinking water for 4 weeks. Control groups received water plus 1.8% (2-hydroxypropyl)-β-cyclodextrin during the treatment period.

After 4 weeks of treatment, behavioral and cognitive tests were performed to study the effects of treatment on working and spatial memory. Drug administration was continued until the euthanasia. Mice were euthanized by cervical dislocation 3 days after the behavioral and cognitive tests were completed. The brains were immediately removed from the skulls, and the hippocampi were dissected, frozen and maintained at −80 °C.

Weight and water consumption were controlled each week, and compounds concentrations were adjusted accordingly to reach the optimal dose. Mice were treated according to European Community Council Directive 86/609/EEC and the studies were approved by the Institutional Animal Care and Use Committee of the University of Barcelona (670/14/8102) and by Generalitat de Catalunya, Spain (10,291). All studies and procedures for the mouse behavioral tests, brain dissection and extractions followed the ARRIVE. Every effort was made to minimize animal suffering and to reduce the number of animals.

4.14.2. Behavioral tests. Novel object recognition test (NORT)

A modification of the NORT protocol was performed [68]. In brief, mice were placed in a 90° two-arm (25 × 20 × 5 cm) black maze, with removable walls for easy cleaning and light intensity in mid-field of 30 lux. Before the memory trials mice were habituated to the apparatus for 10 min for 3 days. On day 4, the animals were

subjected to a 10 min acquisition trial, in which they were allowed to freely explore two identical objects located at the end of each arm (first trial-familiarization). After 2 h (for short-term memory evaluation) and 24 h (for long-term memory evaluation) from the first trial, the mice were subjected to a 10 min retention trial, in which one of the two identical objects had been replaced by a novel one. The behavior was recorded, and the time spent by the mice exploring the new object (TN) and the old one (TO) were measured manually. Exploration was defined as sniffing or touching the objects with the nose and/or forepaws. The discrimination index (DI) was calculated as (TN–TO)/(TN + TO). To avoid object preference biases, objects were alternated. 70% EtOH was used to clean the arms and objects after each trial for the elimination of olfactory cues.

4.14.3. Object location test (OLT)

This test was carried out for 3 days in a wooden box (50 × 50 × 25 cm) with three white walls and one black wall. The first day, the box was empty, and the animals just habituated to the open field arena for 10 min. On the second day, two objects were placed in front of the black wall, equidistant from each other and the wall. The objects were 10-cm high and identical. The animals were placed into the open field arena and allowed to explore both objects and surroundings for 10 min. Thereafter, animals were returned to their home cages, and the OLT apparatus was cleaned with 70% ethanol. On the third day, one object was moved in front of the white wall to test the spatial memory. Trials were recorded using a camera mounted above the open field area, and the total exploration time was determined by scoring the amount of time (s) spent sniffing the object in the new location (TN) and the object in the old location (TO). To evaluate the cognitive performance, the DI was calculated as (TN–TO)/(TN + TO).

4.14.4. Molecular analysis. Western blotting

Western blotting was performed by a standard methodology [10]. After electrophoretic separation (SDS-PAGE, 8−20%) 15 μg of total hippocampal protein were blotted to polyvinylidene difluoride (PVDF) membranes (Millipore, Burlington, MA, USA). Chilled overnight incubation with primary antibodies (Table S7) was performed after blocking membranes in 5% non-fat milk in TRIS-buffered saline (TBS) containing 0.1% Tween 20 (TBS-T, Sigma-Aldrich). Digital images were acquired using a ChemiDoc XRS + System (BioRad lab, Hercules, CA, USA) and analyzed by using ImageLab Software (BioRad Lab). Load control was determined by immunodetection of glyceraldehyde-3-phosphate dehydrogenase (GADPH) inmunodetection. For a more detailed description of the assay see the Supplementary Data.

4.14.5. RNA extraction and determination of gene expression by q-PCR

These techniques were performed by a standard methodology [10]. Real-time quantitative PCR (qPCR) was used to quantify mRNA expression genes listed in Supplementary Table S8, after total RNA isolation and reverse transcription, Data were analyzed by the comparative cycle threshold (Ct) method (ΔΔCt). Housekeeping gen used was β-actin, all samples were analyzed in duplicate. Results were presented as the n-fold difference of the transcript levels among different groups.

4.14.6. Statistical analysis

All data are expressed as the mean ± SEM. Statistical analysis was conducted using GraphPad Prism version 8 statistical software and statistical significance was considered when *p* values were <0.05. All data were tested for normal distribution and equal variance. Group size may vary according to power analysis and

expertise of the authors regarding the behavioral tests [66,67]. Blinded analysis was performed for behavioral tests. Statistical outliers were determined with Grubbs' test and were removed when necessary.

Author contributions

The manuscript was written through contributions of all authors. All authors have given approval to the final version of the manuscript.

Declaration of competing interest

The authors declare that they have no known competing financial interests or personal relationships that could have appeared to influence the work reported in this paper.

Acknowledgements

Appendix A. Supplementary data

Supplementary data to this article can be found online at https://doi.org/10.1016/j.ejmech.2021.113779.

References

[1] Alzheimer's Disease International, World Alzheimer Report 2019: Attitudes to Dementia, Alzheimer's Disease International, London, 2019.

[2] A. Cavalli, M.L. Bolognesi, A. Minarini, M. Rosini, V. Tumiatti, M. Recanatini, C. Melchiorre, Multi-target-directed ligands to combat neurodegenerative diseases, J. Med. Chem. 51 (2008) 347−372, https://doi.org/10.1021/jm7009364.

[3] F. Mesiti, D. Chavarria, A. Gaspar, S. Alcaro, F. Borges, The chemistry toolbox of multitarget-directed ligands for Alzheimer's disease, Eur. J. Med. Chem. 181 (2019) 111572, https://doi.org/10.1016/j.ejmech.2019.111572.

[4] N.F.F. Pirolla, V.S. Batista, F.P. Dias Viegas, V.S. Gontijo, C.R. McCarthy, C. Viegas, N.M. Nascimento-Júnior, Alzheimer's disease: related targets, synthesis of available drugs, bioactive compounds under development and promising results obtained from multi-target approaches, Curr. Drug Targets 22 (2021) 505−538, https://doi.org/10.2174/1389450121999200819144544.

[5] L. Ismaili, J. Monnin, A. Etievant, R.L. Arribas, L. Viejo, B. Refouvelet, O. Soukup, J. Janockova, V. Hepnarova, J. Korabecny, T. Kucera, D. Jun, R. Andrys, K. Musilek, A. Baguet, E.M. García-Frutos, A. De Simone, V. Andrisano, M. Bartolini, C. de los Ríos, J. Marco-Contelles, E. Haffen, (±)-BIGI-3h: pentatarget-directed ligand combining cholinesterase, monoamine oxidase, and glycogen synthase kinase 3β inhibition with calcium channel antagonism and antiaggregating properties for Alzheimer's disease, ACS Chem. Neurosci. 12 (2021) 1328−1342, https://doi.org/10.1021/acschemneuro.0c00803.

[6] A. Pasieka, D. Panek, J. Jończyk, J. Godyń, N. Szałaj, G. Latacz, J. Tabor, E. Mezeiova, F. Chantegreil, J. Dias, D. Knez, J. Lu, R. Pi, J. Korabecny, X. Brazzolotto, S. Gobec, G. Höfner, K. Wanner, A. Więckowska, B. Malawska, Discovery of multifunctional anti-Alzheimer's agents with a unique mechanism of action including inhibition of the enzyme butyrylcholinesterase and γ-aminobutyric acid transporters, Eur. J. Med. Chem. 218 (2021) 113397, https://doi.org/10.1016/j.ejmech.2021.113397.

[7] F. Rodríguez-Enríquez, D. Viña, E. Uriarte, R. Laguna, M.J. Matos, 7-Amido-coumarins as multitarget agents against neurodegenerative diseases: substitution pattern modulation, ChemMedChem 16 (2021) 179−186, https://doi.org/10.1002/cmdc.202000454.

[8] B. Guieu, C. Lecoutey, R. Legay, A. Davis, J. Sopkova de Oliveira Santos, C.D. Altomare, M. Catto, C. Rochais, P. Dallemagne, First synthesis of racemic *trans* propargylamino-donepezil, a pleiotrope agent able to both inhibit AChE

and MAO-B, with potential interest against Alzheimer's disease, Molecules 26 (2020) 80, https://doi.org/10.3390/molecules26010080.

[9] E. Nepovimova, L. Svobodova, R. Dolezal, V. Hepnarova, L. Junova, D. Jun, J. Korabecny, T. Kucera, Z. Gazova, K. Motykova, J. Kubackova, Z. Bednarikova, J. Janockova, C. Jesus, L. Cortes, J. Pina, D. Rostohar, C. Serpa, O. Soukup, L. Aitken, R.E. Hughes, K. Musilek, L. Muckova, P. Jost, M. Chvojkova, K. Vales, M. Valis, Z. Chrienova, K. Chalupova, K. Kuca, Tacrine−benzothiazoles: novel class of potential multitarget anti-Alzheimer's drugs dealing with cholinergic, amyloid and mitochondrial systems, Bioorg. Chem. 107 (2021) 104596, https://doi.org/10.1016/j.bioorg.2020.104596.

[10] F.J. Pérez-Areales, M. Garrido, E. Aso, M. Bartolini, A. De Simone, A. Espargaró, T. Ginex, R. Sabate, B. Pérez, V. Andrisano, D. Puigoriol-Illamola, M. Pallàs, F.J. Luque, M.I. Loza, J. Brea, I. Ferrer, F. Ciruela, A. Messeguer, D. Muñoz-Torrero, Centrally active multitarget anti-Alzheimer agents derived from the antioxidant lead CR-6, J. Med. Chem. 63 (2020) 9360−9390, https://doi.org/10.1021/acs.jmedchem.0c00528.

[11] E. Viayna, N. Coquelle, M. Cieslikiewicz-Bouet, P. Cisternas, C.A. Oliva, E. Sánchez-López, M. Ettcheto, M. Bartolini, A. De Simone, M. Ricchini, M. Rendina, M. Pons, O. Firuzi, B. Pérez, L. Saso, V. Andrisano, F. Nachon, X. Brazzolotto, M.L. García, A. Camins, I. Silman, I. Jean, N.C. Inestrosa, J.-P. Colletier, P.-Y. Renard, D. Muñoz-Torrero, Discovery of a potent dual inhibitor of acetylcholinesterase and butyrylcholinesterase with antioxidant activity that alleviates Alzheimer-like pathology in old APP/PS1 mice, J. Med. Chem. 64 (2021) 812−839, https://doi.org/10.1021/acs.jmedchem.0c01775.

[12] F. He, C.J. Chou, M. Scheiner, E. Poeta, N. Yuan Chen, S. Gunesch, M. Hoffmann, C. Sotriffer, B. Monti, T. Maurice, M. Decker, Melatonin- and ferulic acid-based HDAC6 selective inhibitors exhibit pronounced immunomodulatory effects in vitro and neuroprotective effects in a pharmacological Alzheimer's disease mouse model, J. Med. Chem. 64 (2021) 3794−3812, https://doi.org/10.1021/acs.jmedchem.0c01940.

[13] M. Rossi, M. Freschi, L. de Camargo Nascente, A. Salerno, S. de Melo Viana Teixeira, F. Nachon, F. Chantegreil, O. Soukup, L. Prchal, M. Malaguti, C. Bergamini, M. Bartolini, C. Angeloni, S. Hrelia, L.A. Soares Romeiro, M.L. Bolognesi, Sustainable drug discovery of multi-target-directed ligands for Alzheimer's disease, J. Med. Chem. 64 (2021) 4972−4990, https://doi.org/10.1021/acs.jmedchem.1c00048.

[14] C. Herrera-Arozamena, M. Estrada-Valencia, C. Pérez, L. Lagartera, J.A. Morales-García, A. Pérez-Castillo, J.F. Franco-Gonzalez, P. Michalska, P. Duarte, R. León, M.G. López, A. Mills, F. Gago, Á.J. García-Yagüe, R. Fernández-Ginés, A. Cuadrado, M.I. Rodríguez-Franco, Tuning melatonin receptor subtype selectivity in oxadiazolone-based analogues: discovery of QR2 ligands and NRF2 activators with neurogenic properties, Eur. J. Med. Chem. 190 (2020) 112090, https://doi.org/10.1016/j.ejmech.2020.112090.

[15] M. Pickhardt, Z. Gazova, M. von Bergen, I. Khlistunova, Y. Wang, A. Hascher, E.-M. Mandelkow, J. Biernat, E. Mandelkow, Anthraquinones inhibit tau aggregation and dissolve Alzheimer's paired helical filaments in vitro and in cells, J. Biol. Chem. 280 (2005) 3628−3635, https://doi.org/10.1074/jbc.M410984200.

[16] P. Camps, R. El Achab, J. Morral, D. Muñoz-Torrero, A. Badia, J.E. Baños, N.M. Vivas, X. Barril, M. Orozco, F.J. Luque, New tacrine−huperzine A hybrids (huprines): highly potent tight-binding acetylcholinesterase inhibitors of interest for the treatment of Alzheimer's disease, J. Med. Chem. 43 (2000) 4657−4666, https://doi.org/10.1021/jm000980y.

[17] M.M. Alcalá, N.M. Vivas, S. Hospital, P. Camps, D. Muñoz-Torrero, A. Badia, Characterisation of the anticholinesterase activity of two new tacrine−huperzine A hybrids, Neuropharmacology 44 (2003) 749−755, https://doi.org/10.1016/S0028-3908(03)00071-6.

[18] E. Viayna, I. Sola, M. Bartolini, A. De Simone, C. Tapia-Rojas, F.G. Serrano, R. Sabaté, J. Juárez-Jiménez, B. Pérez, F.J. Luque, V. Andrisano, M.V. Clos, N.C. Inestrosa, D. Muñoz-Torrero, Synthesis and multitarget biological profiling of a novel family of rhein derivatives as disease-modifying anti-Alzheimer agents, J. Med. Chem. 57 (2014) 2549−2567, https://doi.org/10.1021/jm401824w.

[19] F.G. Serrano, C. Tapia-Rojas, F.J. Carvajal, P. Cisternas, E. Viayna, I. Sola, D. Munoz-Torrero, N.C. Inestrosa, Rhein-huprine derivatives reduce cognitive impairment, synaptic failure and amyloid pathology in AβPPswe/PS-1 mice of different ages, Curr. Alzheimer Res. 13 (2016) 1017−1029, https://doi.org/10.2174/1567205012666151027141542.

[20] P. Kacker, G. Bottegoni, A. Cavalli, Computational methods in the discovery and design of BACE-1 inhibitors, Curr. Med. Chem. 19 (2012) 6095−6111.

[21] O. Di Pietro, J. Juárez-Jiménez, D. Muñoz-Torrero, C.A. Laughton, F.J. Luque, Unveiling a novel transient druggable pocket in BACE-1 through molecular simulations: conformational analysis and binding mode of multisite inhibitors, PloS One 12 (2017), e0177683, https://doi.org/10.1371/journal.pone.0177683.

[22] G. Novak, J.R. Streffer, M. Timmers, D. Henley, H.R. Brashear, J. Bogert, A. Russu, L. Janssens, I. Tesseur, L. Tritsmans, L. Van Nueten, S. Engelborghs, Long-term safety and tolerability of atabecestat (JNJ-54861911), an oral BACE1 inhibitor, in early Alzheimer's disease spectrum patients: a randomized, double-blind, placebo-controlled study and a two-period extension study, Alzheimer's Res. Ther. 12 (2020) 58, https://doi.org/10.1186/s13195-020-00614-5.

[23] L. McConlogue, M. Buttini, J.P. Anderson, E.F. Brigham, K.S. Chen, S.B. Freedman, D. Games, K. Johnson-Wood, M. Lee, M. Zeller, W. Liu, R. Motter, S. Sinha, Partial reduction of BACE1 has dramatic effects on

[24] Alzheimer plaque and synaptic pathology in APP transgenic mice, J. Biol. Chem. 282 (2007) 26326−26334, https://doi.org/10.1074/jbc.M611687200.

[24] M. Maia, E. Sousa, BACE-1 and γ-secretase as therapeutic targets for Alzheimer's disease, Pharmaceuticals 12 (2019) 41, https://doi.org/10.3390/ph12010041.

[25] H. Hampel, R. Vassar, B. De Strooper, J. Hardy, M. Willem, N. Singh, J. Zhou, R. Yan, E. Vanmechelen, A. De Vos, R. Nisticò, M. Corbo, B.P. Imbimbo, J. Streffer, I. Voytyuk, M. Timmers, A.A. Tahami Monfared, M. Irizarry, B. Albala, A. Koyama, N. Watanabe, T. Kimura, L. Yarenis, S. Lista, L. Kramer, A. Vergallo, The β-secretase BACE1 in Alzheimer's disease, Biol. Psychiatr. 89 (2021) 745−756, https://doi.org/10.1016/j.biopsych.2020.02.001.

[26] F. Prati, G. Bottegoni, M.L. Bolognesi, A. Cavalli, BACE-1 inhibitors: from recent single-target molecules to multitarget compounds for Alzheimer's disease: Miniperspective, J. Med. Chem. 61 (2018) 619−637, https://doi.org/10.1021/acs.jmedchem.7b00393.

[27] A. Iraji, M. Khoshneviszadeh, O. Firuzi, M. Khoshneviszadeh, N. Edraki, Novel small molecule therapeutic agents for Alzheimer disease: focusing on BACE1 and multi-target directed ligands, Bioorg. Chem. 97 (2020) 103649, https://doi.org/10.1016/j.bioorg.2020.103649.

[28] J.R.M. Coimbra, S.J. Baptista, T.C.P. Dinis, M.M.C. Silva, P.I. Moreira, A.E. Santos, J.A.R. Salvador, Combining virtual screening protocol and in vitro evaluation towards the discovery of BACE1 inhibitors, Biomolecules 10 (2020) 535, https://doi.org/10.3390/biom10040535.

[29] G. Bottegoni, M. Veronesi, P. Bisignano, P. Kacker, A.D. Favia, A. Cavalli, Development and application of a virtual screening protocol for the identification of multitarget fragments, ChemMedChem 11 (2016) 1259−1263, https://doi.org/10.1002/cmdc.201500521.

[30] F.J. Pérez-Areales, N. Betari, A. Viayna, C. Pont, A. Espargaró, M. Bartolini, A. De Simone, J.F. Rinaldi Alvarenga, B. Pérez, R. Sabate, R.M. Lamuela-Raventós, V. Andrisano, F.J. Luque, D. Muñoz-Torrero, Design, synthesis and multitarget biological profiling of second-generation anti-Alzheimer rhein−huprine hybrids, Future Med. Chem. 9 (2017) 965−981, https://doi.org/10.4155/fmc-2017-0049.

[31] M.J. Abraham, D. van der Spoel, E. Lindahl, B. Hess, the Gromacs development team, GROMACS User Manual Version, 2018. www.gromacs.org.

[32] T.W. Johnson, R.A. Gallego, M.P. Edwards, Lipophilic efficiency as an important metric in drug design, J. Med. Chem. 61 (2018) 6401−6420, https://doi.org/10.1021/acs.jmedchem.8b00077.

[33] S. Darvesh, Butyrylcholinesterase as a diagnostic and therapeutic target for Alzheimer's disease, Curr. Alzheimer Res. 13 (2016) 1173−1177, https://doi.org/10.2174/1567205013666160402120542.

[34] Q. Li, Y. Chen, S. Xing, Q. Liao, B. Xiong, Y. Wang, W. Lu, S. He, F. Feng, W. Liu, Y. Chen, H. Sun, Highly potent and selective butyrylcholinesterase inhibitors for cognitive improvement and neuroprotection, J. Med. Chem. 64 (2021) 6856−6876, https://doi.org/10.1021/acs.jmedchem.1c00167.

[35] M. Hoffmann, C. Stiller, E. Endres, M. Scheiner, S. Gunesch, C. Sotriffer, T. Maurice, M. Decker, Highly selective butyrylcholinesterase inhibitors with tunable duration of action by chemical modification of transferable carbamate units exhibit pronounced neuroprotective effect in an Alzheimer's disease mouse model, J. Med. Chem. 62 (2019) 9116−9140, https://doi.org/10.1021/acs.jmedchem.9b01012.

[36] Q. Li, S. Xing, Y. Chen, Q. Liao, B. Xiong, S. He, W. Lu, Y. Liu, H. Yang, Q. Li, F. Feng, W. Liu, Y. Chen, H. Sun, Discovery and biological evaluation of a novel highly potent selective butyrylcholinsterase inhibitor, J. Med. Chem. 63 (2020) 10030−10044, https://doi.org/10.1021/acs.jmedchem.0c01129.

[37] M. Bortolami, D. Rocco, A. Messore, R. Di Santo, R. Costi, V.N. Madia, L. Scipione, F. Pandolfi, Acetylcholinesterase inhibitors for the treatment of Alzheimer's disease − a patent review (2016−present), Expert Opin. Ther. Pat. 31 (2021) 399−420, https://doi.org/10.1080/13543776.2021.1874344.

[38] G.L. Ellman, K.D. Courtney, V. Andres, R.M. Featherstone, A new and rapid colorimetric determination of acetylcholinesterase activity, Biochem. Pharmacol. 7 (1961) 88−95, https://doi.org/10.1016/0006-2952(61)90145-9.

[39] A. Espargaró, C. Pont, P. Gamez, D. Muñoz-Torrero, R. Sabate, Amyloid pan-inhibitors: one family of compounds to cope with all conformational diseases, ACS Chem. Neurosci. 10 (2019) 1311−1317, https://doi.org/10.1021/acschemneuro.8b00398.

[40] C. Galdeano, E. Viayna, I. Sola, X. Formosa, P. Camps, A. Badia, M.V. Clos, J. Relat, M. Ratia, M. Bartolini, F. Mancini, V. Andrisano, M. Salmona, C. Minguillón, G.C. González-Muñoz, M.I. Rodríguez-Franco, A. Bidon-Chanal, F.J. Luque, D. Muñoz-Torrero, Huprine−tacrine heterodimers as anti-amyloidogenic compounds of potential interest against Alzheimer's and prion diseases, J. Med. Chem. 55 (2012) 661−669, https://doi.org/10.1021/jm200840c.

[41] P. Camps, X. Formosa, C. Galdeano, D. Muñoz-Torrero, L. Ramírez, E. Gómez, N. Isambert, R. Lavilla, A. Badia, M.V. Clos, M. Bartolini, F. Mancini, V. Andrisano, M.P. Arce, M.I. Rodríguez-Franco, Ó. Huertas, T. Dafni, F.J. Luque, Pyrano[3,2-c]quinoline−6-chlorotacrine hybrids as a novel family of acetylcholinesterase- and β-amyloid-directed anti-Alzheimer compounds, J. Med. Chem. 52 (2009) 5365−5379, https://doi.org/10.1021/jm900859q.

[42] O. Di Pietro, F.J. Pérez-Areales, J. Juárez-Jiménez, A. Espargaró, M.V. Clos, B. Pérez, R. Lavilla, R. Sabaté, F.J. Luque, D. Muñoz-Torrero, Tetrahydrobenzo[h][1,6]naphthyridine-6-chlorotacrine hybrids as a new family of anti-Alzheimer agents targeting β-amyloid, tau, and cholinesterase pathologies, Eur. J. Med. Chem. 84 (2014) 107−117, https://doi.org/10.1016/j.ejmech.2014.07.021.

[43] A. Espargaró, A. Medina, O. Di Pietro, D. Muñoz-Torrero, R. Sabate, Ultra rapid in vivo screening for anti-Alzheimer anti-amyloid drugs, Sci. Rep. 6 (2016) 23349, https://doi.org/10.1038/srep23349.

[44] Y. Li, Q. Jiao, H. Xu, X. Du, L. Shi, F. Jia, H. Jiang, Biometal dyshomeostasis and toxic metal accumulations in the development of Alzheimer's disease, Front. Mol. Neurosci. 10 (2017) 339, https://doi.org/10.3389/fnmol.2017.00339.

[45] P.-P. Liu, Y. Xie, X.-Y. Meng, J.-S. Kang, History and progress of hypotheses and clinical trials for Alzheimer's disease, Signal Transduct. Target Ther. 4 (2019) 29, https://doi.org/10.1038/s41392-019-0063-8.

[46] M. Rosini, E. Simoni, A. Milelli, A. Minarini, C. Melchiorre, Oxidative stress in Alzheimer's disease: are we connecting the dots? J. Med. Chem. 57 (2014) 2821–2831, https://doi.org/10.1021/jm400970m.

[47] M.G. Savelieff, A.S. DeToma, J.S. Derrick, M.H. Lim, The ongoing search for small molecules to study metal-associated amyloid-β species in Alzheimer's disease, Acc. Chem. Res. 47 (2014) 2475–2482, https://doi.org/10.1021/ar500152x.

[48] Z. Wang, J. Hu, X. Yang, X. Feng, X. Li, L. Huang, A.S.C. Chan, Design, synthesis, and evaluation of orally bioavailable quinoline–indole derivatives as innovative multitarget-directed ligands: promotion of cell proliferation in the adult murine hippocampus for the treatment of Alzheimer's disease, J. Med. Chem. 61 (2018) 1871–1894, https://doi.org/10.1021/acs.jmedchem.7b01417.

[49] Z. Yang, Q. Song, Z. Cao, G. Yu, Z. Liu, Z. Tan, Y. Deng, Design, synthesis and evaluation of flurbiprofen-clioquinol hybrids as multitarget-directed ligands against Alzheimer's disease, Bioorg. Med. Chem. 28 (2020) 115374, https://doi.org/10.1016/j.bmc.2020.115374.

[50] D. Chavarria, O. Da Silva, S. Benfeito, S. Barreiro, J. Garrido, F. Cagide, P. Soares, F. Remião, X. Brazzolotto, F. Nachon, P.J. Oliveira, J. Dias, F. Borges, Fine-tuning the biological profile of multitarget mitochondriotropic antioxidants for neurodegenerative diseases, Antioxidants 10 (2021) 329, https://doi.org/10.3390/antiox10020329.

[51] J.S. Santos, V.R. Alvarenga Brizola, D. Granato, High-throughput assay comparison and standardization for metal chelating capacity screening: a proposal and application, Food Chem. 214 (2017) 515–522, https://doi.org/10.1016/j.foodchem.2016.07.091.

[52] D. Huang, B. Ou, R.L. Prior, The chemistry behind antioxidant capacity assays, J. Agric. Food Chem. 53 (2005) 1841–1856, https://doi.org/10.1021/jf030723c.

[53] S. Tan, D. Schubert, P. Maher, Oxytosis: a novel form of programmed cell death, Curr. Top. Med. Chem. 1 (2001) 497–506, https://doi.org/10.2174/1568026013394741.

[54] OECD, Test No. 236: Fish Embryo Acute Toxicity (FET) Test; OECD Guidelines for the Testing of Chemicals, Section 2, OECD, 2013, https://doi.org/10.1787/9789264203709-en.

[55] C.A. MacRae, R.T. Peterson, Zebrafish as tools for drug discovery, Nat. Rev. Drug Discov. 14 (2015) 721–731, https://doi.org/10.1038/nrd4627.

[56] G.R. Garcia, P.D. Noyes, R.L. Tanguay, Advancements in zebrafish applications for 21st century toxicology, Pharmacol. Ther. 161 (2016) 11–21, https://doi.org/10.1016/j.pharmthera.2016.03.009.

[57] A.J. Hill, H. Teraoka, W. Heideman, R.E. Peterson, Zebrafish as a model vertebrate for investigating chemical toxicity, Toxicol. Sci. 86 (2005) 6–19, https://doi.org/10.1093/toxsci/kfi110.

[58] M. Barenys, A. Molins, L. Amorós-Galicia, B. Flick, J. Gómez-Catalán, Implementation of a functional endpoint to the zebrafish embryotoxicity test to evaluate craniofacial abnormalities, Toxicol. Vitro 61 (2019) 104638, https://doi.org/10.1016/j.tiv.2019.104638.

[59] L. Di, E.H. Kerns, K. Fan, O.J. McConnell, G.T. Carter, High throughput artificial membrane permeability assay for blood–brain barrier, Eur. J. Med. Chem. 38 (2003) 223–232, https://doi.org/10.1016/S0223-5234(03)00012-6.

[60] E.H. Kerns, L. Di, Drug-like Properties: Concepts, Structure Design and Methods: from ADME to Toxicity Optimization, Academic Press, Amsterdam; Boston, 2008, pp. 56–85.

[61] K.A. Dehring, H.L. Workman, K.D. Miller, A. Mandagere, S.K. Poole, Automated robotic liquid handling/laser-based nephelometry system for high throughput measurement of kinetic aqueous solubility, J. Pharmaceut. Biomed. Anal. 36 (2004) 447–456, https://doi.org/10.1016/j.jpba.2004.07.022.

[62] J.E. Morley, H.J. Armbrecht, S.A. Farr, V.B. Kumar, The senescence accelerated mouse (SAMP8) as a model for oxidative stress and Alzheimer's disease, Biochim. Biophys. Acta 1822 (2012) 650–656, https://doi.org/10.1016/j.bbadis.2011.11.015.

[63] J.E. Morley, S.A. Farr, V.B. Kumar, H.J. Armbrecht, The SAMP8 mouse: a model to develop therapeutic interventions for Alzheimer's disease, Curr. Pharmaceut. Des. 18 (2012) 1123–1130, https://doi.org/10.2174/138161212799315795.

[64] T. Takeda, Senescence-accelerated mouse (SAM) with special references to neurodegeneration models, SAMP8 and SAMP10 mice, Neurochem. Res. 34 (2009) 639–659, https://doi.org/10.1007/s11064-009-9922-y.

[65] M. Pallàs, Senescence-accelerated mice P8: a tool to study brain aging and Alzheimer's disease in a mouse model, ISRN Cell Biol 2012 (2012) 1–12, https://doi.org/10.5402/2012/917167.

[66] C. Griñán-Ferré, V. Palomera-Ávalos, D. Puigoriol-Illamola, A. Camins, D. Porquet, V. Plá, F. Aguado, M. Pallàs, Behaviour and cognitive changes correlated with hippocampal neuroinflammaging and neuronal markers in female SAMP8, a model of accelerated senescence, Exp. Gerontol. 80 (2016) 57–69, https://doi.org/10.1016/j.exger.2016.03.014.

[67] C. Griñán-Ferré, R. Corpas, D. Puigoriol-Illamola, V. Palomera-Ávalos, C. Sanfeliu, M. Pallàs, Understanding epigenetics in the neurodegeneration of

[68] Alzheimer's disease: SAMP8 mouse model, J. Alzheimers Dis. 62 (2018) 943–963, https://doi.org/10.3233/JAD-170664.

[68] J. Companys-Alemany, A.L. Turcu, A. Bellver-Sanchis, M.I. Loza, J.M. Brea, A.M. Canudas, R. Leiva, S. Vázquez, M. Pallàs, C. Griñán-Ferré, A novel NMDA receptor antagonist protects against cognitive decline presented by senescent mice, Pharmaceutics 12 (2020) 284, https://doi.org/10.3390/pharmaceutics12030284.

[69] V.W. Chow, M.P. Mattson, P.C. Wong, M. Gleichmann, An overview of APP processing enzymes and products, NeuroMolecular Med. 12 (2010) 1–12, https://doi.org/10.1007/s12017-009-8104-z.

[70] M.O.W. Grimm, J. Mett, C.P. Stahlmann, V.J. Haupenthal, V.C. Zimmer, T. Hartmann, Neprilysin and Aβ clearance: impact of the APP intracellular domain in NEP regulation and implications in Alzheimer's disease, Front. Aging Neurosci. 5 (2013), https://doi.org/10.3389/fnagi.2013.00098.

[71] W. Farris, S. Mansourian, Y. Chang, L. Lindsley, E.A. Eckman, M.P. Frosch, C.B. Eckman, R.E. Tanzi, D.J. Selkoe, S. Guenette, Insulin-degrading enzyme regulates the levels of insulin, amyloid β-protein, and the β-amyloid precursor protein intracellular domain in vivo, Proc. Natl. Acad. Sci. U.S.A. 100 (2003) 4162–4167, https://doi.org/10.1073/pnas.0230450100.

[72] A.A. Turab Naqvi, G.M. Hasan, Mdl. Hassan, Targeting tau hyperphosphorylation via kinase inhibition: strategy to address Alzheimer's disease, Curr. Top. Med. Chem. 20 (2020) 1059–1073, https://doi.org/10.2174/1568026622066620010615210.

[73] G. Plascencia-Villa, G. Perry, Preventive and therapeutic strategies in Alzheimer's disease: focus on oxidative stress, redox metals, and ferroptosis, Antioxidants Redox Signal. 34 (2021) 591–610, https://doi.org/10.1089/ars.2020.8134.

[74] S. Sánchez-Sarasúa, I. Fernández-Pérez, V. Espinosa-Fernández, A.M. Sánchez-Pérez, J.C. Ledesma, Can we treat neuroinflammation in Alzheimer's disease? Int. J. Mol. Sci. 21 (2020) 8751, https://doi.org/10.3390/ijms21228751.

[75] B. Liu, J. Liu, J.-S. Shi, SAMP8 mice as a model of age-related cognition decline with underlying mechanisms in Alzheimer's disease, J. Alzheimers Dis. 75 (2020) 385–395, https://doi.org/10.3233/JAD-200063.

[76] K.-S. Yoo, K. Lee, J.-Y. Oh, H. Lee, H. Park, Y.S. Park, H.K. Kim, Postsynaptic density protein 95 (PSD-95) is transported by KIF5 to dendritic regions, Mol. Brain 12 (2019) 97, https://doi.org/10.1186/s13041-019-0520-x.

[77] S. Takamori, M. Holt, K. Stenius, E.A. Lemke, M. Grønborg, D. Riedel, H. Urlaub, S. Schenck, B. Brügger, P. Ringler, S.A. Müller, B. Rammner, F. Gräter, J.S. Hub, B.L. De Groot, G. Mieskes, Y. Moriyama, J. Klingauf, H. Grubmüller, J. Heuser, F. Wieland, R. Jahn, Molecular anatomy of a trafficking organelle, Cell 127 (2006) 831–846, https://doi.org/10.1016/j.cell.2006.10.030.

[78] F.N.B. Edfeldt, R.H.A. Folmer, A.L. Breeze, Fragment screening to predict druggability (ligandability) and lead discovery success, Drug Discov. Today 16 (2011) 284–287, https://doi.org/10.1016/j.drudis.2011.02.002.

[79] J.J. Irwin, T. Sterling, M.M. Mysinger, E.S. Bolstad, R.G. Coleman, ZINC: a free tool to discover chemistry for biology, J. Chem. Inf. Model. 52 (2012) 1757–1768, https://doi.org/10.1021/ci3001277.

[80] L.L.C. Schrödinger, Schrödinger Release 2017-3, Schrödinger LLC, New York, NY, USA, 2017.

[81] R.A. Friesner, R.B. Murphy, M.P. Repasky, L.L. Frye, J.R. Greenwood, T.A. Halgren, P.C. Sanschagrin, D.T. Mainz, Extra precision Glide: docking and scoring incorporating a model of hydrophobic enclosure for protein–ligand complexes, J. Med. Chem. 49 (2006) 6177–6196, https://doi.org/10.1021/jm051256o.

[82] A. Tarozzi, M. Bartolini, L. Piazzi, L. Valgimigli, R. Amorati, C. Bolondi, A. Djemil, F. Mancini, V. Andrisano, A. Rampa, From the dual function lead AP2238 to AP2469, a multi-target-directed ligand for the treatment of Alzheimer's disease, Pharmacol. Res. Perspect. 2 (2014) e00023, https://doi.org/10.1002/prp2.23.

[83] J. Wang, R.M. Wolf, J.W. Caldwell, P.A. Kollman, D.A. Case, Development and testing of a general amber force field, J. Comput. Chem. 25 (2004) 1157–1174, https://doi.org/10.1002/jcc.20035.

[84] J. Wang, P. Cieplak, P.A. Kollman, How well does a restrained electrostatic potential (RESP) model perform in calculating conformational energies of organic and biological molecules? J. Comput. Chem. 21 (2000) 1049–1074, https://doi.org/10.1002/1096-987X(200009)21:12<1049::AID-JCC3>3.0.CO;2-F.

[85] M.J. Frisch, G.W. Trucks, H.B. Schlegel, G.E. Scuseria, M.A. Robb, J.R. Cheeseman, G. Scalmani, V. Barone, B. Mennucci, G.A. Petersson, H. Nakatsuji, M. Caricato, X. Li, H.P. Hratchian, A.F. Izmaylov, J. Bloino, G. Zheng, J.L. Sonnenberg, M. Hada, M. Ehara, K. Toyota, R. Fukuda, J. Hasegawa, M. Ishida, T. Nakajima, Y. Honda, O. Kitao, H. Nakai, T. Vreven, J.A. Montgomery Jr., J.E. Peralta, F. Ogliaro, M. Bearpark, J.J. Heyd, E. Brothers, K.N. Kudin, V.N. Staroverov, R. Kobayashi, J. Normand, K. Raghavachari, A. Rendell, J.C. Burant, S.S. Iyengar, J. Tomasi, M. Cossi, N. Rega, J.M. Millam, M. Klene, J.E. Knox, J.B. Cross, V. Bakken, C. Adamo, J. Jaramillo, R. Gomperts, R.E. Stratmann, O. Yazyev, A.J. Austin, R. Cammi, C. Pomelli, J.W. Ochterski, R.L. Martin, K. Morokuma, V.G. Zakrzewski, G.A. Voth, P. Salvador, J.J. Dannenberg, S. Dapprich, A.D. Daniels, Ö. Farkas, J.B. Foresman, J.V. Ortiz, J. Cioslowski, D.J. Fox, Gaussian 09, Gaussian, Inc., Wallingford CT, 2009.

[86] V. Hornak, R. Abel, A. Okur, B. Strockbine, A. Roitberg, C. Simmerling, Comparison of multiple Amber force fields and development of improved protein backbone parameters, Proteins 65 (2006) 712–725, https://doi.org/10.1002/prot.21123.

[87] K. Lindorff-Larsen, S. Piana, K. Palmo, P. Maragakis, J.L. Klepeis, R.O. Dror,

D.E. Shaw, Improved side-chain torsion potentials for the Amber ff99SB protein force field: improved Protein Side-Chain Potentials, Proteins 78 (2010) 1950−1958, https://doi.org/10.1002/prot.22711.

[88] W.L. Jorgensen, J. Chandrasekhar, J.D. Madura, R.W. Impey, M.L. Klein, Comparison of simple potential functions for simulating liquid water, J. Chem. Phys. 79 (1983) 926−935, https://doi.org/10.1063/1.445869.

[89] G. Bussi, D. Donadio, M. Parrinello, Canonical sampling through velocity rescaling, J. Chem. Phys. 126 (2007), 014101, https://doi.org/10.1063/1.2408420.

[90] M. Parrinello, A. Rahman, Polymorphic transitions in single crystals: a new molecular dynamics method, J. Appl. Phys. 52 (1981) 7182−7190, https://doi.org/10.1063/1.328693.

[91] B. Hess, H. Bekker, H.J. Berendsen, J.G. Fraaije, LINCS: a linear constraint solver for molecular simulations, J. Comput. Chem. 18 (1997) 1463−1472, https://doi.org/10.1002/(SICI)1096-987X(199709)18:12<1463::AID-JCC4>3.0.CO;2-H.

[92] T. Darden, D. York, L. Pedersen, Particle mesh Ewald: an $N \cdot \log(N)$ method for Ewald sums in large systems, J. Chem. Phys. 98 (1993) 10089−10092, https://doi.org/10.1063/1.464397.

[93] T. Sander, J. Freyss, M. von Korff, C. Rufener, DataWarrior: an open-source program for chemistry aware data visualization and analysis, J. Chem. Inf. Model. 55 (2015) 460−473, https://doi.org/10.1021/ci500588j.

[94] ChemAxon. https://chemaxon.com/products/calculators-and-predictorschemaxon.com, 2021.

[95] S. Pouplana, A. Espargaró, C. Galdeano, E. Viayna, I. Sola, S. Ventura, D. Muñoz-Torrero, R. Sabate, Thioflavin-S staining of bacterial inclusion bodies for the fast, simple, and inexpensive screening of amyloid aggregation inhibitors, Curr. Med. Chem. 21 (2014) 1152−1159, https://doi.org/10.2174/09298673113206660256.